

# LABORATORY PRACTICUM: DOSIMETRY AND GAMMA SPECTROMETRY

BAKSAN 2025

Nikolay Anfimov, Alexander Selyunin  
Laboratory of Nuclear Problems  
Joint Institute for Nuclear Research

# Contents

<b>INTRODUCTION</b>	<b>2</b>
<b>1 Radioactivity</b>	<b>3</b>
1.1 Beta Decay . . . . .	3
1.2 Alpha Decay . . . . .	4
1.3 Gamma Radiation . . . . .	7
<b>2 Units of measurement</b>	<b>10</b>
<b>3 Methods of Radiation Detection</b>	<b>14</b>
3.1 Geiger Counter . . . . .	14
3.2 Scintillators . . . . .	21
3.3 Photomultiplier Tube . . . . .	30
3.3.1 Photocathode . . . . .	31
3.3.2 Dynode System of PMT . . . . .	34
3.3.3 Gain Coefficient . . . . .	36
3.3.4 PMT Noise . . . . .	36
<b>4 Experimental Setup</b>	<b>38</b>
4.1 Software . . . . .	39
4.2 Laboratory Practical. Work Procedure . . . . .	42

# Introduction

Gamma radiation accompanies nuclear transformations in the vast majority of radionuclides. The nucleus formed during radioactive decay is most often in an excited state ( $E_{ex}$ ). When it transitions to a lower energy level or the ground state ( $E_g$ ), a  $\gamma$ -quantum is emitted. The energy of these quanta ( $E_\gamma = E_{ex} - E_g$ ) is determined by the structure of the energy levels of a given nucleus. Consequently, the  $\gamma$  spectrum acts as a unique "fingerprint" of the radionuclide. Therefore, gamma spectrometry – the determination of the energy spectrum of  $\gamma$ -quanta emitted by the investigated substance – is the most universal method for identifying radionuclides in samples of various compositions. Gamma spectrometry is also an important component of many instrumental methods of chemical analysis. For example, the  $\gamma$ -spectra of nuclides formed during neutron irradiation of a complex sample make it possible to determine the content of various chemical elements in the studied material.

# Chapter 1

## Radioactivity

The activity of any radioisotope is determined by its decay rate and is expressed by the fundamental law of radioactive decay:

$$\frac{dN}{dt} = -\lambda N, \quad (1.1)$$

where  $N$  is the number of radioactive nuclei, and  $\lambda$  is the decay constant, which characterizes the probability of radioactive decay. This law essentially means that the number of decays  $dN$  occurring over a short time interval  $dt$  is proportional to the number of atoms  $N$  in the material. Historically, the unit of radioactivity was the Curie (denoted Ci), equal to  $3.7 \cdot 10^{10}$  decays per second, corresponding to the activity of 1 g of  $^{226}\text{Ra}$ . In 1975, the General Conference on Weights and Measures adopted a new unit of radioactivity: the becquerel (Bq), defined as one decay per second:  $1 \text{ Bq} = 2.703 \cdot 10^{-11} \text{ Ci}$ .

### 1.1 Beta Decay

Radioactive isotopes that undergo  $\beta^-$ -decay are commonly used as sources of fast electrons:



In this equation,  $X$  and  $Y$  are the initial and final products of the reaction,  $\beta^-$  is the negatively charged beta particle (electron), and  $\bar{\nu}$  is the antineutrino. The probability of antineutrino interaction with the surrounding environment is extremely low, so these particles are not detected in most conventional experiments.

Beta decay does not change the nucleon number  $A$  but changes only the nuclear charge  $Z$ . Most natural isotopes are beta-stable, but some isotopes with long half-lives can still be found in nature, such as  $^{40}\text{K}$ , which undergoes both beta-minus and beta-plus decay, as well as electron capture. The decay scheme

of this isotope is shown in Figure 1.1. However, most radioisotopes used in scientific and industrial applications are produced by bombarding stable materials with neutrons, resulting in beta-active isotopes. A large number of beta isotopes are obtained through reactor channels. The primary beta sources are listed in Table 1.1. In most cases, beta decay leads to the population of an excited state of the daughter nucleus, followed by de-excitation with the emission of gamma radiation along with beta particles.

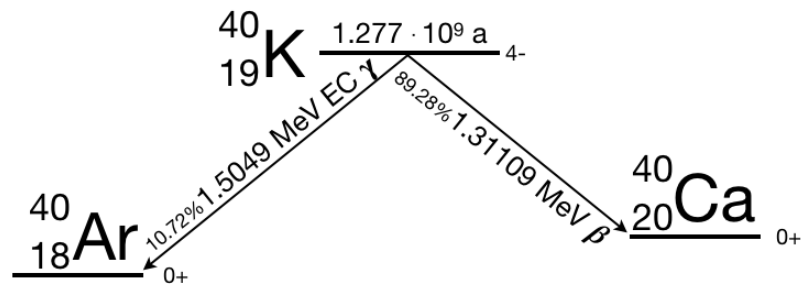


Figure 1.1: The decay scheme of  $^{40}\text{K}$

Transitions in beta decay are characterized by a fixed decay energy or Q-value. Since the recoil nucleus energy is practically zero, the energy is distributed between beta particles and the "invisible" neutrino. Thus, beta particles have energy that varies from one decay event to another. The beta decay energy spectrum is continuous and ranges from zero to the "maximum beta decay energy," which numerically equals the Q-value. The beta decay spectrum is shown in Figure 1.2. It is worth noting that the shape of the beta radiation spectrum is significantly influenced by the atomic Coulomb field, which consists of the nucleus field and the electron shell field. The distortion introduced into the spectrum by the atomic field is particularly significant at the beginning of the spectrum, i.e., for beta particles with low energy. In this case, the center of gravity of the energy spectrum shifts toward lower energies for electrons and higher energies for positrons. This shift increases with the nuclear charge.

## 1.2 Alpha Decay

Heavy nuclei are energetically unstable with respect to the spontaneous emission of alpha particles (the nucleus of a helium atom,  $^4_2\text{He}$ ). The probability of decay is determined by the likelihood of an alpha particle penetrating the Coulomb barrier in the nucleus. We will not delve into this effect in detail, as it is described in many textbooks on nuclear physics. The half-life of alpha particle sources ranges from a few days to thousands of years. The decay process can be schematically

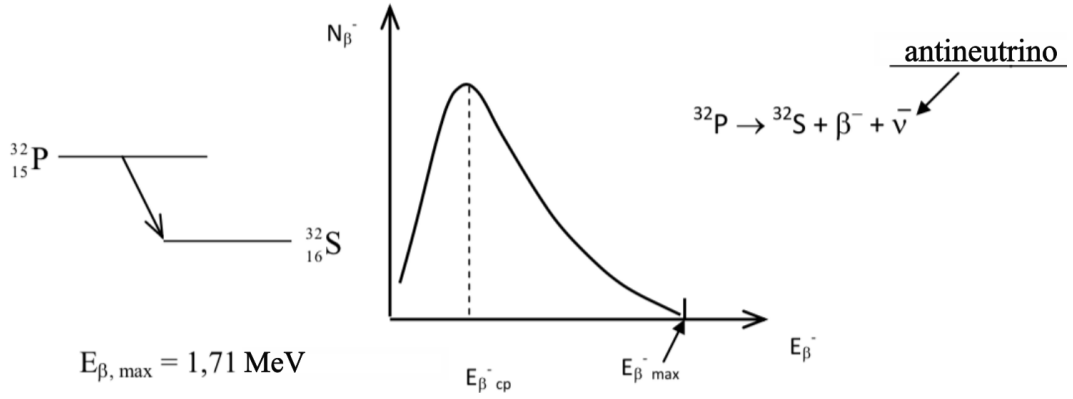


Figure 1.2: The decay scheme of  $^{32}\text{P}$  and the spectrum of emitted  $\beta^-$  particles.

Table 1.1: **Widely used  $\beta^-$  isotopes**

Isotop	Half-life	Maximum decay energy, MeV
$^3\text{H}$	12,26 years	0,0186
$^{14}\text{C}$	5730 years	0,156
$^{32}\text{P}$	14,28 d.	1,710
$^{33}\text{P}$	24,4 d.	0,248
$^{35}\text{S}$	87,9 d.	0,167
$^{36}\text{Cl}$	$3,08 \cdot 10^5$ years	0,714
$^{40}\text{K}$	$1,28 \cdot 10^9$ years	1,311
$^{45}\text{Ca}$	165 d.	0,252
$^{65}\text{Ni}$	92 y.	0,067
$^{90}\text{Sr}/^{90}\text{Y}$	27,7 years/64 h.	0,546/2,270
$^{147}\text{Pm}$	2,62 y.	0,224
$^{204}\text{Tm}$	3,81 y.	0,766

described as follows:

$${}^A_Z X \rightarrow {}^{A-4}_{Z-2} Y + {}^4_2 \alpha, \quad (1.3)$$

where  $X$  and  $Y$  are the initial and final decay products, respectively. Alpha particles produced during nuclear decay are monoenergetic and have an initial kinetic energy in the range of 1.8 to 15 MeV. As the alpha particle moves through matter, it loses energy very quickly and thus can be absorbed by a simple sheet of paper or even a layer of air.

Table 1.2 lists the characteristics of the main radioisotopes that are sources of alpha particles. The energy of alpha particles from most alpha-emitting sources lies in the range of 3 to 6 MeV. It should be noted that there is a correlation between the energy of the alpha particle and the half-life of the source – the higher the energy of the particle, the shorter the half-life. Isotopes that emit alpha particles with energies above 6.5 MeV have a half-life of only a few days, which limits their applications. On the other hand, if the energy of the alpha particle

is below 4 MeV, the probability of its emission from the nucleus (overcoming the Coulomb barrier) is quite low, and thus the lifetime of such an isotope is significantly longer. The activity of long-lived isotopes is also substantially lower.

The most commonly used calibration sources of alpha particles are  $^{241}\text{Am}$  and  $^{239}\text{Pu}$ . For example,  $^{241}\text{Am}$  is widely used for calibrating semiconductor detectors. As mentioned, alpha particles lose energy rapidly in matter, so alpha-emitting sources are manufactured as thin layers coated with metal foil or other protective materials to shield the source.

Table 1.2: Main sources of  $\alpha$ -particles.

Isotop	Half-life	Kinetic energy of $\alpha$ -particles, MeV	Percentage share
$^{148}\text{Gd}$	93 years	3,18	100
$^{232}\text{Th}$	$1,4 \cdot 10^{10}$ years	4,012	77
		3,953	23
$^{238}\text{U}$	$4,5 \cdot 10^9$ years	4,196	77
		4,149	23
$^{235}\text{U}$	$7,1 \cdot 10^8$ years	4,598	4,6
		4,401	56
		4,374	6
		4,365	12
		4,219	6
$^{236}\text{U}$	$2,4 \cdot 10^7$ years	4,494	74
		4,445	26
$^{230}\text{Th}$	$7,7 \cdot 10^4$ years	4,688	76,3
		4,62	23,4
$^{234}\text{U}$	$2,5 \cdot 10^5$ years	4,77	72
		4,72	28
$^{239}\text{U}$	$2,4 \cdot 10^4$ years	5,155	73,3
		5,143	15,1
		5,105	11,5
$^{240}\text{U}$	$6,5 \cdot 10^3$ years	5,168	76
		5,124	24
$^{210}\text{Po}$	133 days	5,305	99+
$^{241}\text{Am}$	433 years	5,486	85,2
		5,443	12,8
$^{238}\text{Pu}$	88 years	5,499	71,1
		5,457	28,8
$^{242}\text{Cm}$	163 days	6,113	74
		6,07	26
$^{253}\text{Es}$	20,5 days	6,633	90
		6,592	6,6

### 1.3 Gamma Radiation

Gamma radiation is emitted from an excited nucleus as it transitions to lower-energy states or the ground state. In most commonly used laboratory sources, excited states are formed during the decay of the parent isotope. Figure 1.3 shows the decay schemes of two of the most widely used sources of gamma radiation:  $^{60}\text{Co}$  and  $^{137}\text{Cs}$ . In both isotopes, beta decay leads to the population of an excited state in the daughter nucleus. The lifetime of the nucleus in the excited state is significantly shorter than the lifetime of the parent isotope. The de-excitation process occurs with the emission of a gamma quantum with energy equal to the difference between the energies of the ground and excited states of the daughter nucleus. Thus, the gamma radiation energy spectrum will have a discrete structure that characterizes the energy structure of the daughter nucleus, while the radiation intensity is determined by the half-life of the parent nucleus. For example, the intensity of gamma radiation from  $^{60}\text{Co}$  decreases according to the decay of  $^{60}\text{Co}$  (half-life of 5.26 years), but the energy spectrum (lines at 1.33 MeV and 1.17 MeV) characterizes the structure of the  $^{60}\text{Ni}$  nucleus. The transition probabilities in the decay scheme can be used to estimate the number of decays accompanied by gamma-ray emission in the parent nucleus. The discrete nature of the gamma radiation energy spectrum allows various isotopes to be used as calibration sources. A list of such sources is given in Table 1.3.

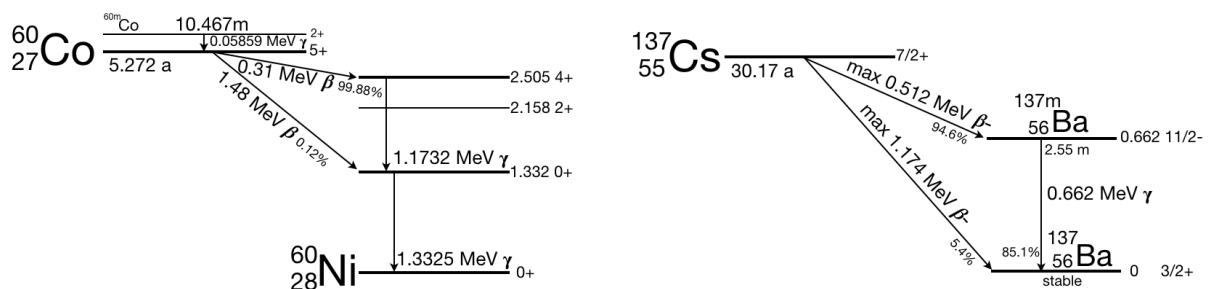


Figure 1.3: Decay of isotopes  $^{137}\text{Cs}$  and  $^{60}\text{Co}$ .

The gamma radiation energy of commonly used gamma sources does not exceed 2.8 MeV. Using the isotope  $^{56}\text{Co}$ , gamma quanta with energies up to 3.55 MeV can be obtained; however, the half-life of this material is only 77 days, which limits its widespread application. For the calibration of detectors with higher energies, the isotope  $^{16}\text{N}$  is used, with gamma radiation energies of 6.13 and 7.11 MeV, emitted during beta decay to  $^{16}\text{O}$ . However, the lifetime of  $^{16}\text{N}$  is only 7 seconds. Such isotopes are produced exclusively in reactors or accelerators. The radioactivity of laboratory calibration sources of gamma radiation is low. Typically, the isotope

activity does not exceed a few microcuries (approximately  $10^5$  Bq).

Table 1.3: Main sources of  $\gamma$ -radiation.

Isotop	$T_{1/2}$	E, keV	I(%)
$^{22}\text{Na}$	2,6 y.	1274,5	99,95
$^{40}\text{K}$	$1,23 \cdot 10^9$ years	1460	10,72
$^{60}\text{Co}$	5,27 years	1173	99,88
		1332	99,98
$^{133}\text{Ba}$	10,5 years	31	64,5
		81	34
		302	18
		356	62
$^{137}\text{Cs}$	30,2 y.	32	5,64
		662	85,3
$^{226}\text{Ra}$	1600 years	186	3,59
$^{214}\text{Pb}$	26,8 min	242	16
		295	42
		352	80
$^{214}\text{Bi}$	19,9 min	609	100
		768	10,9
		934	6,93
		1120	32,72
		1238	12,94
		1378	8,87
		1509	4,78
		1730	6,29
		1765	34,23
		1847	4,52
		2204	10,77
$^{208}\text{Tl}$	3 min	511	22,6
		583	84,5
		2615	99
$^{212}\text{Pb}$	10,6 h	239	43,3
$^{228}\text{Ac}$	6,15 h	338	11,3
		911	25,8
		969	15,8
$^{241}\text{Am}$	432 y.	59,5	36

## Chapter 2

# Units of measurement

When exposed to radiation, processes of ionization and excitation of atoms occur in human organs and tissues as a result of energy absorption, representing the biological effects of radiation. The measure of this effect is the amount of energy absorbed by the organism. Different types of radiation are characterized by varying biological effectiveness due to differences in their penetrating ability and the way energy is transferred to the organs and tissues of a living organism, which consists mainly of light elements. The effect of radiation exposure depends on the magnitude of the absorbed dose, its dose rate, the type of radiation, and the volume of tissue and organs exposed.

Table 2.1: Main radiological quantities and units

Quantity	Name (non-SI)	Name (SI)	Unit conversion ratio
Nuclide activity, A	Curie (Ci)	Becquerel (Bq)	1 Ci = $3.7 \cdot 10^{10}$ Bq 1 Bq = 1 decay/s
Exposure dose, X	Roentgen (R)	Coulomb per kilogram (C/kg)	1 R = $2.58 \cdot 10^{-4}$ C/kg 1 C/kg = $3.88 \cdot 10^3$ R
Absorbed dose, D	Rad (rad)	Gray (Gy)	1 rad = $10^{-2}$ Gy 1 Gy = 1 J/kg
Equivalent dose, H	Ber (rem)	Sievert (Sv)	1 rem = $10^{-2}$ Sv
Integral radiation dose	Rad-gram (rad·g)	Gray-kilogram (Gy·kg)	1 rad·g = $10^{-5}$ Gy·kg

To describe the effects of ionizing radiation on matter, the following concepts and measurement units are used:

**Activity of a radionuclide in a source (A).** The activity is defined as the ratio of the number of spontaneous nuclear transformations in the source during a small time interval ( $dN$ ) to the duration of this interval ( $dt$ ):

$$A = dN/dt \quad (2.1)$$

The unit of activity in the SI system is the Becquerel (Bq). The non-SI unit is the Curie (Ci). The number of radioactive nuclei  $N(t)$  of a given isotope decreases over time according to the law:

$$N(t) = N_0 \cdot e^{-t \cdot \frac{\ln 2}{T_{1/2}}} = N_0 \cdot e^{-t \cdot \frac{0.693}{T_{1/2}}} \quad (2.2)$$

where  $N_0$  is the number of radioactive nuclei at time  $t = 0$ , and  $T_{1/2}$  is the half-life — the time during which half of the radioactive nuclei decay.

**Exposure dose (X).** As a quantitative measure of X-ray and  $\gamma$ -radiation, the exposure dose is used in non-SI units, defined by the charge of secondary particles ( $dQ$ ) produced in a mass of material ( $dm$ ) when all charged particles are fully stopped:

$$X = dQ/dm \quad (2.3)$$

The unit of exposure dose is the Roentgen (R). A Roentgen is defined as the exposure dose of X-rays and  $\gamma$ -radiation that creates, in  $1\text{cm}^3$  of air at a temperature of  $0^\circ\text{C}$  and a pressure of 760 mmHg, a total ion charge of one sign equal to one electrostatic unit of electric charge. An exposure dose of 1 R corresponds to  $2.08 \cdot 10^9$  ion pairs ( $2.08 \cdot 10^9 = 1/(4.8 \cdot 10^{-10})$ ). If we take the average energy required to form one ion pair in air as 33.85 eV, then, at an exposure dose of 1 R, the energy transferred to one cubic centimeter of air is:

$$(2.08 \cdot 10^9) \cdot 33.85 \cdot (1.6 \cdot 10^{-19}) = 0.113 \cdot 10^{-7} \text{ J} = 0.113 \text{ erg},$$

and to one gram of air:

$$0.113/\rho_{air} = 0.113/0.001293 = 87.3 \text{ erg}.$$

The absorption of energy from ionizing radiation is the primary process that initiates a sequence of physico-chemical transformations in the irradiated tissue, leading to the observed radiation effect. Therefore, it is natural to associate the observed effect with the amount of absorbed energy or absorbed dose.

**Absorbed Dose (D)** – the main dosimetric quantity. It is defined as the ratio of the mean energy  $dE$  imparted by ionizing radiation to a substance in an elementary volume to the mass  $dm$  of the substance in that volume:

$$D = dE/dm \quad (2.4)$$

The unit of absorbed dose is the Gray (Gy). The non-SI unit Rad was defined as the absorbed dose of any ionizing radiation equal to 100 ergs per gram of irradiated substance.

**Equivalent Dose (H).** To assess the potential harm to human health in conditions of chronic exposure in the field of radiation safety, the concept of equivalent dose  $H$  was introduced. It is defined as the product of the absorbed dose  $D_r$ , created by radiation  $r$  and averaged over the analyzed organ or the whole body, and the weighting factor  $w_r$  (also known as the radiation quality factor) (see Table 2.2):

$$H = \sum_r w_r \cdot D_r \quad (2.5)$$

The unit of equivalent dose is the Joule per kilogram, with the special name Sievert (Sv).

Table 2.2: **Radiation weighting factors**

The type of radiation and the energy range	weighting factor
Photons of all energies	1
Electrons and muons of all energies	1
Neutrons with energy $\leq 10$ keV	5
Neutrons from 10 to 100 keV	10
Neutrons from 100 keV to 2 MeV	20
Neutrons from 2 MeV to 20 MeV	10
Neutrons $\geq 20$ MeV	5
Protons with energy $\geq 2$ MeV (except recoil protons)	5
$\alpha$ -particles, fission fragments, and other heavy nuclei	20

The impact of irradiation is uneven. To assess the health damage caused by the different effects of radiation on various organs (in the case of uniform irradiation of the entire body), the concept of effective dose  $E_{eff}$  has been introduced, which is used when evaluating potential stochastic effects — malignant neoplasms.

**The effective dose** is the sum of the weighted equivalent doses in all organs and tissues:

$$E_{eff} = \sum_t w_t \cdot H_t \quad (2.6)$$

where  $w_t$  is the tissue weighting factor (table 2.3), and  $H_t$  is the equivalent dose absorbed in the tissue  $t$ . The unit of the effective equivalent dose is Sievert.

**Comparison of doses.** There are different types of doses – exposure, absorbed, and equivalent doses. The units of measurement for doses are also different – roentgen and coulomb/kg, rad and gray, sievert and rem. Household dosimeters show the dose rate in microroentgen per hour ( $\mu\text{R}/\text{hour}$ ), while, for example, accident reports may use microsievert per hour ( $\mu\text{Sv}/\text{hour}$ ) or millisieverts per hour ( $\text{mSv}/\text{hour}$ ). Although exposure dose is not the same as equivalent

Table 2.3: The values of tissue weighting factors  $w_t$  for various organs and tissues.

Tissue or organ	$w_t$	Tissue or organ	$w_t$
Gonads	0.20	Liver	0.05
Red bone marrow	0.12	Esophagus	0.05
Large intestine	0.12	Thyroid gland	0.05
Lungs	0.12	Skin	0.01
Stomach	0.12	Bone surface	0.01
Bladder	0.05	Other organs	0.05
Mammary glands	0.05	-	-

dose, in most cases of interest to non-professionals, the following relationship can be used:

$$100 \mu\text{R} \approx 1 \mu\text{Sv},$$

$$100 \text{ rem} = 1 \text{ Sv}.$$

The dose rate in Moscow is usually 13-15  $\mu\text{R}/\text{hour}$ . Radiation is divided into external and internal types. External radiation is caused by sources located outside the human body. Sources of external radiation include cosmic radiation and terrestrial sources. Internal radiation is caused by radionuclides present in the human body.

Let's consider examples of equivalent doses:

- 1-2 Sv (instantaneously) causes severe radiation poisoning, more than 2 Sv is a lethal dose.
- X-ray of the hand – 1-5  $\mu\text{Sv}$
- X-ray of the chest – 100  $\mu\text{Sv}$
- Fluorography – 300  $\mu\text{Sv}$
- Mammography – 700  $\mu\text{Sv}$
- CT scan of the chest – 7 mSv, head – 2 mSv, whole body – 10 mSv.
- Airplane flight – tens of  $\mu\text{Sv}$  (depends on altitude and flight duration)
- The global average dose from natural sources accumulated per capita per year is 2.4 mSv, with a range from 1 to 10 mSv.

## Chapter 3

# Methods of Radiation Detection

### 3.1 Geiger Counter

Geiger-Müller counters<sup>1</sup> are among the most widely used detectors of ionizing radiation, alongside ionization chambers and proportional counters. The counter was invented in 1908 by German physicist Geiger (H. Geiger) and English physicist Rutherford (E. Rutherford), and was improved in 1913 by German physicist Müller (W. Müller). It is primarily used for detecting X-rays and cosmic rays, as well as  $\beta$ - and  $\gamma$ -radiation. Geiger-Müller counters played an important role in nuclear physics in the 1920s–1940s, and are currently predominantly used in dosimetry.

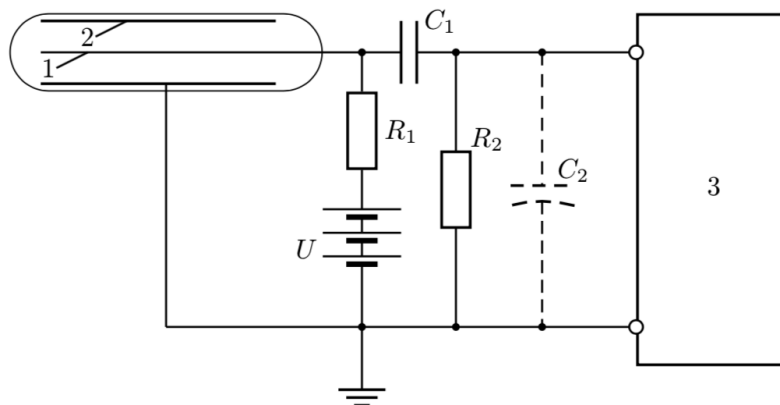


Figure 3.1: Geiger-Müller counter circuit diagram

**Construction.** The device itself consists of a sealed chamber (usually made of glass), filled with an inert gas at a pressure of 13–26 kPa. Therefore, all the above-mentioned counters are called gas-filled detectors. Inside the chamber are electrodes under high voltage, creating a highly non-uniform electric field. In practice, cylindrical counters are more commonly used (see Fig.3.3a). The circuit

<sup>1</sup>Materials taken from source [1]

diagram of such a counter is shown in Fig.3.1. The inner electrode (anode) 1 is a thin straight tungsten wire with a diameter of 0.1 mm, insulated from the chamber walls. The outer electrode (cathode) 2 is located along the cylindrical walls, and if the chamber is made of glass, it is applied as a coating on the walls (copper, tungsten, nichrome, steel, etc.).

**Circuit diagram.** A high voltage ( $U \sim 300 \div 1000$  V) is applied between the anode and cathode, with the cathode grounded. The capacitor  $C_1$  separates the high-voltage power circuit of the counter from the input circuit of the electronic circuit. The resistor  $R_1$  ( $R_1 \sim 10^8 \div 10^9$  Ohms) isolates the anode from the power supply, which reduces the potential of the wire during the discharge.

The change in the anode potential is registered by an electronic counting device. The pulse amplitude when registering a particle is approximately 1 V, so the counting devices do not require significant amplification of the input signal.

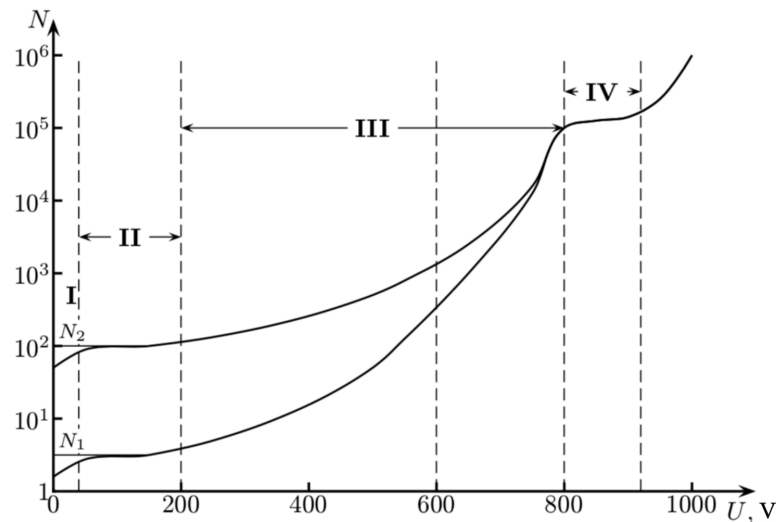


Figure 3.2: Dependence of the number of collected ion pairs on the applied voltage. The curves correspond to two different types of particles, creating  $N_1$  and  $N_2$  ion pairs in the counter volume, respectively.

**Principle of operation.** Suppose a particle passes through the volume of the counter and creates  $N$  ion pairs in it. Figure 3.2 shows the dependence of the number of ion pairs collected by the electrodes of the counter on the applied voltage. Two curves are given for different particles creating  $N_1$  and  $N_2$  ion pairs. These curves can be divided into 4 main sections.

In section I, there are two competing processes: charge collection on the electrodes and ion recombination. As the voltage increases, the speed of electron movement increases, the probability of recombination decreases, and the amount of collected charge increases.

At a certain voltage, all ions (for these curves,  $N_1$  and  $N_2$ ) formed by the

particle will settle on the electrodes, and the number of pairs will not increase with further voltage increase. This situation corresponds to the saturation current in section II. The collected charge in this section is determined only by the ionization capacity of the registered particle. This section is called the ionization chamber region — the amount of charge collected by the anode is equal to the total charge of electrons formed by the particle during ionization. The ionization chamber operates in the range from several volts to 200 V and is designed for detecting "bursts" of particles, with "bursts" from different particles differing from each other.

In section III, the collected charge increases by a factor  $K$  due to gas amplification: electrons created by primary ionization accelerate in the electric field and gain enough energy to cause secondary (impact) ionization. At the beginning of section III, the amplification factor does not depend on the initial ionization, and the charge collected on the electrodes is proportional to the number of ion pairs created by the charged particle. The part of the curve where gas amplification occurs but the charge still depends on the initial ionization is called the proportional region, and proportional counters operate in this region. As the voltage increases, this proportionality is gradually violated, and at the end of section III, the pulse amplitude becomes independent of the initial ionization; this part is called the limited proportionality region.

In section IV, the collected charge does not depend on the initial ionization. In a highly non-uniform electric field, electrons are rapidly accelerated, acquiring enough energy for ionization. The number of electrons increases in an avalanche-like manner, and near the anode, the entire gas becomes ionized, creating what is known as a corona discharge. Thus, the charge increases to a value determined by the characteristics of the chamber and external circuitry. With further increase in the applied voltage, the region of impact ionization expands, and the voltage pulse on the anode slightly increases. However, the discharge remains forced, and the curve practically stops growing. This section is called the Geiger-Müller region. Counters operating in region IV are called Geiger-Müller counters, see Fig. 3.3.

Geiger-Müller counters are distinguished by their high sensitivity: any particle passing through the counter will be registered if it creates at least one ion pair (neutrons,  $\gamma$ -quanta, and X-rays are detected through secondary ionizing particles). On the other hand, these counters cannot determine the energy or type of particles.

**Efficiency.** The efficiency of a counter is the ratio of the number of registered



Figure 3.3: Geiger-Müller Counters. a – cylindrical, b – end-window, c – pancake

particles to the total number of particles that passed through the counter. A particle passing through the counter may not create an ion pair, or the formed ions may diffuse into a non-operating area of the counter.

Thus, the efficiency depends on the design and materials of the counter and differs for various types of particles. For electrons, efficiency can reach 99–99.9%. Registration of  $\gamma$ -quanta occurs due to secondary ionization;  $\gamma$ -quanta create Compton electrons or electron-positron pairs (for energies  $E_\gamma > 1,022$  MeV). The efficiency of counters for  $\gamma$ -rays is about 1%.

**Discharge mechanism in Geiger-Müller counters.** In the Geiger-Müller region, each electron on its way to the anode creates a certain number of ion pairs and excites some atoms. An avalanche of electrons, formed by the primary particle, reaches the anode. However, excited atoms return to the normal state by emitting photons, which, in turn, knock photoelectrons off the cathodes; ions reaching the cathode can also knock electrons out. As a result of these processes, a second avalanche is created, then a third, and so on. This leads to an ongoing discharge. In reality, such a discharge will eventually stop: the speed of ions is much slower than that of electrons, and their number equals the number of electrons created, resulting in a large positive volume charge that reduces the field strength and suppresses secondary processes. Such a counter becomes practically unusable as it can only register one particle over a long interval.

To increase the efficiency of counters, it is necessary to quench the secondary discharge process (in a normally operating counter, the discharge should stop after the first avalanche). There are self-quenching and non-self-quenching Geiger-Müller counters.

External quenching circuit: To quench the secondary discharge in regular counters, a resistance  $R_1 \sim 10^9$  is used in the anode circuit of the counter's connection scheme (fig. 3.1). Thus, the time constant (RC) of the input circuit is much larger than the time required to collect positive ions. During the discharge, the ionization process stops as soon as the potential between the anode and cathode drops below the critical value. A disadvantage of such counters is their low resolving capability,  $\gtrsim 10^{-3}$  s.

Self-quenching counters: One method of quenching the secondary discharge is the addition of organic polyatomic gases with low ionization potentials and small electron attachment coefficients (e.g., alcohol vapors, ethylene, methylene). These gases can absorb ultraviolet light and neutralize ions from inert gases. As a result, the ions of organic molecules, rather than the inert gas, are neutralized at the cathode. After recombination, the molecules, in an excited state, disintegrate very quickly ( $\sim 10^{-13}$  seconds) into smaller molecules or composite atoms, without having enough time to emit a photon or knock off an electron from the surface of the cathode. Organic molecules do not have the ability to regenerate, and therefore such counters experience "aging" (a deterioration of the counter's characteristics), and are designed to last for approximately  $10^{10}$  pulses.

Another type of self-quenching counters is halogen counters, which do not have this drawback. In these counters, a small amount (0.1%) of halogen ( $\text{Br}_2$ ,  $\text{Cl}_2$ ,  $\text{J}_2$ ) is added to the working gas. The quenching mechanism with halogens is similar to the one described above, except that halogen molecules later recombine. Halogen counters have a low operating voltage (about 300 V).

**Counting characteristic.** The counting characteristic is the relationship between the counting rate and the applied voltage (with constant ionizing radiation intensity). The counting characteristic depends on many factors, such as the diameter of the anode, the composition and pressure of the gas, etc. An example of such a curve is shown in Fig. 3.4.

The voltage at which counting begins (the counting threshold) corresponds to the minimum pulse amplitudes that can be registered by the electronic circuit. The initial segment of the counting characteristic corresponds to the limited proportionality region.

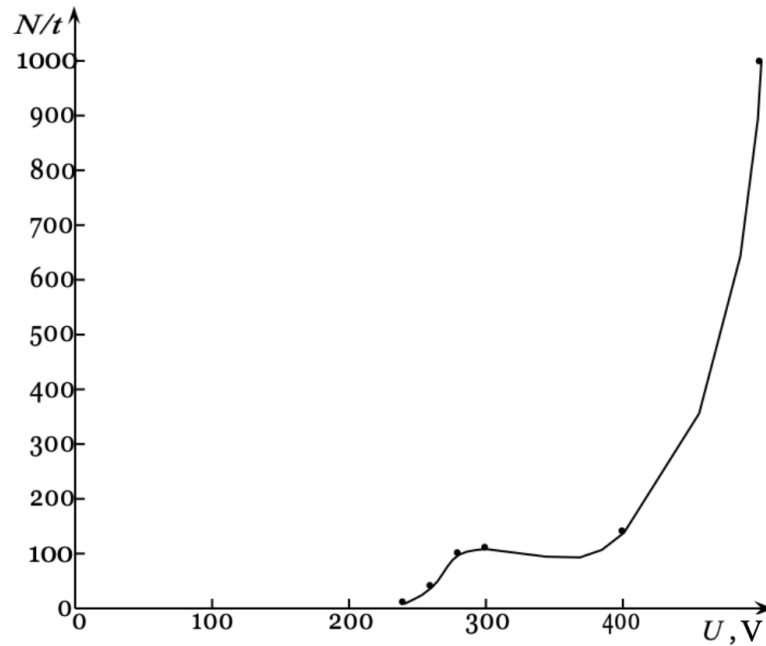


Figure 3.4: Counting characteristic of the Geiger-Müller counter

Starting from a certain voltage, the counting rate is approximately independent of the applied voltage; in this region, each particle that creates at least one ion pair generates a pulse with an amplitude sufficient for detection. This section is called the plateau region. The length of the plateau is usually several hundred volts. The slope of the plateau is due to the presence of secondary electrons (knocked out of the cathode), which create false pulses, and a slight increase in the sensitive volume of the counter with increasing voltage. Typically, the slope is a few percent per 100 V. The working voltage is chosen in the middle of the plateau.

Further increases in voltage lead to "breakdown" of the counter – particle passing through the detector volume cause an ongoing avalanche of electrons and ions (due to secondary electrons knocked out from the cathode walls by electrons and ions). This section of the curve is called the continuous discharge region.

**Resolving Time of Geiger-Müller Counters.** The speed of positive ions in a Geiger-Müller counter is much slower than that of electrons. As a result, for some time after a discharge, due to the presence of a volumetric positive charge, the electric field in the counter is insufficient to ionize the gas. Particles entering the counter during this period will not be registered! This time interval is called the resolving or dead time of the counter. After the dead time has passed, particles will be registered again, but with a reduced signal amplitude (see Fig. 3.5). The time interval required for the full restoration of the pulse amplitude after the dead time ends is called the recovery time. The typical value of the dead time is

approximately  $\sim 10^{-4}$  s.

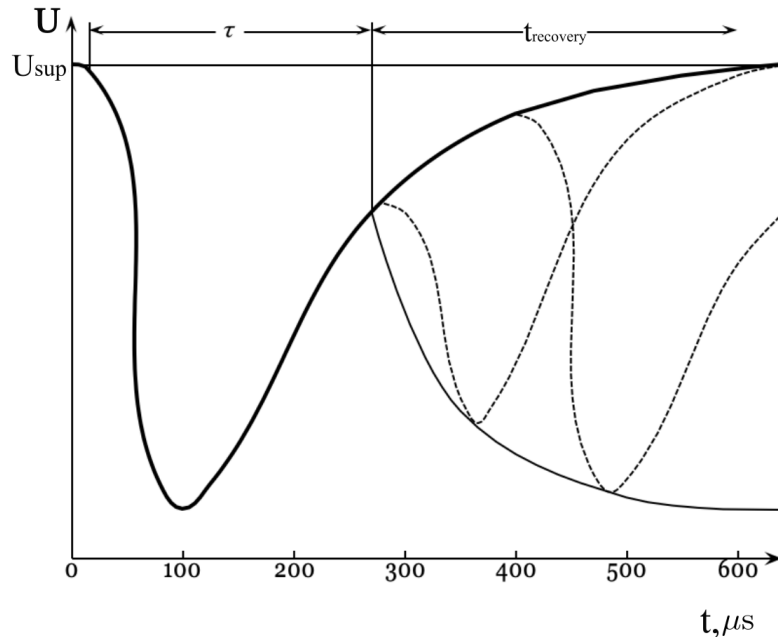


Figure 3.5: Voltage pulse on the collecting electrode.  $\tau$  - dead time,  $t_{\text{rec}}$  - recovery time. Dashed lines represent pulses from particles entering during the counter's recovery period, showing reduced amplitude.

If, over a certain period (for simplicity, take 1 s), the counter registers  $n$  particles, then for  $n\tau$  s the counter does not register any particles, where  $\tau$  is the dead time. Thus, instead of the "true" number of particles  $n_0$ , the counter registers:

$$n = n_0(1 - n\tau) \quad (3.1)$$

From which we get:

$$n_0 = \frac{n}{1 - n\tau} \quad (3.2)$$

The dead time of the counter can be determined experimentally using the multiple-source method. Suppose we measure the count rates ( $\dot{n}_i = n_i/t_i$ ) for each  $\beta$ -source individually and for the case when all sources are open ( $\dot{n}_\Sigma = n_\Sigma/t_\Sigma$ ). For such an experiment, we can write:

$$\dot{n}_{0_\Sigma} = \sum_{i=1}^k \dot{n}_{0_i} \quad (3.3)$$

where  $k$  is the number of sources. However, considering the background radiation, along with each  $n_0$ , the counter also detects  $n_{0_\Phi}$ . Then equation (3.2) can be rewritten as:  $\dot{n}_{0_\Sigma} - \dot{n}_{0_\Phi} = (\dot{n}_{0_1} - \dot{n}_{0_\Phi}) + (\dot{n}_{0_2} - \dot{n}_{0_\Phi}) + \dots + (\dot{n}_{0_k} - \dot{n}_{0_\Phi})$ , or

$$\dot{n}_{0_\Sigma} = \sum_{i=1}^k \dot{n}_{0_i} - (k - 1)\dot{n}_{0_\Phi} \quad (3.4)$$

Substituting equation (3.1) into this, we get:

$$\frac{\dot{n}_\Sigma}{1 - \dot{n}_\Sigma\tau} = \sum_{i=1}^k \frac{\dot{n}_i}{1 - \dot{n}_i\tau} - (k-1) \frac{\dot{n}_\Phi}{1 - \dot{n}_\Phi\tau} \quad (3.5)$$

Since  $\dot{n}\tau \ll 1$ , we can simplify to:

$$\tau = \frac{\sum_{i=1}^k \dot{n}_i - \dot{n}_\Sigma - (k-1)\dot{n}_\Phi}{\dot{n}_\Sigma^2 + (k-1)\dot{n}_\Phi^2 - \sum_{i=1}^k \dot{n}_i^2} \quad (3.6)$$

### 3.2 Scintillators

The main characteristics of scintillators are: light yield, spectral composition of radiation, and duration of scintillations.

When a charged particle passes through a scintillator, a certain number of photons with varying energies are generated within it. Some of these photons will be absorbed within the volume of the scintillator itself, and instead, other photons with slightly lower energy will be emitted. As a result of reabsorption processes, the photons that emerge outward will have a spectrum characteristic of the given scintillator.

The light yield or conversion efficiency of a scintillator is defined as the ratio of the energy of the light flash exiting the scintillator to the energy  $E$  lost by the charged particle in the scintillator:

$$\chi = \frac{\bar{n}h\bar{\nu}}{E} \quad (3.7)$$

where  $\bar{n}$  is the average number of photons exiting the scintillator, and  $h\bar{\nu}$  is the average energy of the photons. Each scintillator emits not monoenergetic quanta but a continuous spectrum of the given scintillator.

It is very important that the spectrum of photons exiting the scintillator matches or at least partially overlaps with the spectral response of the photomultiplier tube (PMT). The degree of overlap between the external scintillation spectrum and the spectral characteristic  $\varepsilon(\nu)$  of a given PMT is determined by the matching coefficient:

$$K = \frac{\int_0^\infty F(\nu)\varepsilon(\nu)d\nu}{\int_0^\infty F(\nu)d\nu} \quad (3.8)$$

where  $F(\nu)$  is the external spectrum of the scintillator or the spectrum of photons exiting the scintillator. In practice, when comparing scintillators combined with

specific PMTs, the concept of scintillation efficiency is introduced, which is defined by the following expression:

$$A = K\chi \quad (3.9)$$

Scintillation efficiency takes into account both the number of photons emitted by the scintillator per unit of absorbed energy and the sensitivity of the PMT to these photons. Typically, the scintillation efficiency of a given scintillator is determined by comparison with the scintillation efficiency of a reference scintillator.

The intensity of scintillation changes over time according to an exponential law:

$$I(t) = I_0 e^{-\frac{t}{\tau}} \quad (3.10)$$

where  $I_0$  is the maximum value of scintillation intensity, and  $\tau$  is the decay time constant, defined as the time during which the scintillation intensity decreases by a factor of  $e$ .

The number of light photons  $n$  emitted during time  $t$  after the detection of a particle is expressed by the formula:

$$n = n_0 \left(1 - e^{-\frac{t}{\tau}}\right) \quad (3.11)$$

where  $n_0$  is the total number of photons emitted during the scintillation process.

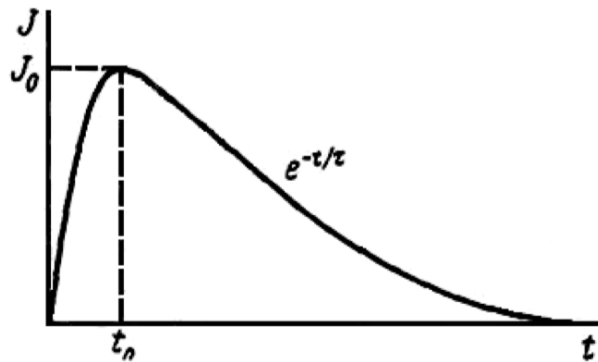


Figure 3.6: The dependence of the phosphor's luminescence intensity on time

Phosphorus luminescence processes are divided into two types: fluorescence and phosphorescence. If the illumination occurs directly during excitation or over a time interval of about  $10^{-8}$  seconds, the process is called fluorescence. The interval of  $10^{-8}$  seconds is chosen because it is equal in order of magnitude to the lifetime of an atom in the excited state for the so-called allowed transitions. Although the fluorescence spectra and duration do not depend on the type of excitation, the fluorescence yield significantly depends on it. Thus, when the crystal is excited by  $\alpha$  particles, the fluorescence yield is almost an order of magnitude lower than during photoexcitation. Phosphorescence is understood as luminescence, which lasts

for a considerable time after the cessation of excitation. But the main difference between fluorescence and phosphorescence is not the duration of the afterglow. Phosphorescence of crystallophosphores occurs when electrons and holes formed during excitation recombine. In some crystals, it is possible to prolong the afterglow due to the fact that electrons and holes are trapped by "traps" from which they can be released only by receiving additional necessary energy. Hence, the dependence of the duration of phosphorescence on temperature is obvious. In the case of complex organic molecules, phosphorescence is associated with their stay in a metastable state, the probability of transition from which to the ground state may be low. In this case, the phosphorescence attenuation rate will depend on temperature.

Scintillation detectors are based on the detection of luminescence caused by the action of radiation on luminophore, in which the radiation energy is converted into light flashes (scintillations). The luminophors used for these purposes are commonly referred to as scintillators.

Various substances (solid, liquid, and gaseous) are used as scintillators. The scintillator can be organic (crystals, plastics, or liquids) or inorganic (crystals or glasses). Gaseous scintillators are also used.

**Inorganic Scintillators.** Inorganic scintillators are crystals of inorganic salts. In scintillation technology, halide compounds of certain alkali metals are mainly used. To increase the light yield of such scintillators, special impurities of other elements, called activators (e.g., thallium), are introduced. A scintillator based on a NaI(Tl) crystal has a high light output.

Solid-state inorganic scintillators include NaCl(AgCl), NaI (activated with Tl), LiI(Eu), LiF(Eu), CsI(Tl), KI(Tl),  $\text{Bi}_4\text{Ge}_3\text{O}_{12}$  (BGO), and others. All these materials allow the growth of large crystals, which are subsequently processed accordingly. These scintillators are used for detecting  $\gamma$ -radiation, as they have a high average atomic number  $Z$  and high density. CsI crystals have low hygroscopicity, making them suitable for use in scintillation counters even in atmospheric conditions. The listed scintillators have relatively similar decay times of about  $10^{-6}$  seconds, which mainly determines the timing resolution of detectors based on them.

A relatively new type of scintillator is based on bismuth germanate oxide (BGO). With a higher density than NaI, BGO detectors have significantly greater efficiency in detecting  $\gamma$ -radiation, especially in the high-energy range. For example, to achieve the same measurement accuracy in spectrometers based on BGO

and NaI, the latter requires an exposure time increased by a factor of 3.3. However, BGO has drawbacks, such as low light output and relatively poor resolution compared to traditional scintillators. Cadmium tungstate crystals ( $\text{CdWO}_4$ , CWO) are expected to be introduced into radiometry, as they outperform BGO in several characteristics. With high detection efficiency, CWO scintillators provide better resolution, higher light yield, and weak dependence on ambient temperature.

Lanthanum bromide scintillation crystals doped with cerium,  $\text{LaBr}_3(\text{Ce})$ , have higher energy resolution and shorter decay times than traditional  $\text{NaI}(\text{Tl})$  crystals. For  $\gamma$ -radiation energy of 662 keV, their energy resolution is 2.9% (19 keV), whereas for a  $\text{NaI}(\text{Tl})$  crystal of similar size under the same conditions, the resolution is 6%. Additionally,  $\text{LaBr}_3(\text{Ce})$  offers higher detection efficiency and good temperature stability. Detection devices based on  $\text{LaBr}_3(\text{Ce})$  allow for confident analysis of samples with complex gamma spectra. High resolution directly improves radionuclide identification quality in studied samples, reduces the minimum detectable activity for identical measurement times, and consequently shortens the required sample measurement duration. The high temperature stability of such detectors enables their effective use under extreme temperature conditions.

There are many efficient scintillators that, however, cannot be grown into large crystals for detectors. For example,  $\text{ZnS}(\text{Tl})$  has low hygroscopicity and high conversion efficiency, reaching 20–25%, which is nearly independent of the energy of registered particles.  $\text{ZnS}(\text{Ag})$  is used for  $\alpha$ -radiation detection. Zinc sulfide is widely used in detector production as a fine crystalline powder applied in a thin layer on a transparent substrate, such as acrylic glass. These detectors have a relatively long resolving time of  $10^{-3}$  seconds but are successfully used for detecting heavy charged particles. If a boron-containing component, such as  $\text{B}_2\text{O}_3$ , is added to such a powder, an efficient detector for detecting slow and thermal neutrons can be obtained via the nuclear reaction  ${}^{10}_5\text{B}(\text{n},\alpha){}_2^3\text{Li}$ , with low sensitivity to accompanying  $\gamma$ -radiation.

Detectors based on  $\text{LiI}$  and  $\text{LiF}$  doped with  ${}^6\text{Li}$  are also suitable for detecting slow and thermal neutrons. Neutrons induce the reaction  ${}^6\text{Li}(\text{n},\alpha)\text{T}$ , producing high-energy particles. However, these detectors also register  $\gamma$  background, which can subsequently be discriminated in the detection apparatus.

The scintillation process can be described using the band theory of solid state. In an isolated atom that does not interact with others, electrons occupy discrete energy levels. In a solid, atoms are positioned closely, and their interaction is significant. Due to this interaction, the energy levels of outer electron shells split

into bands separated by forbidden energy gaps. The outermost allowed band occupied by electrons is called the valence band, while the conduction band is located above it. Between the valence and conduction bands is the forbidden band, whose energy width is several electron volts.

If there are defects, lattice distortions, or impurity atoms in the crystal, additional electronic energy levels may appear within the forbidden band. When exposed to external influences, such as a fast-charged particle passing through the crystal, electrons may transition from the valence band to the conduction band, leaving vacant positions in the valence band called holes, which behave as positively charged particles.

This process is the excitation of the crystal. The excitation is quenched by the reverse transition of electrons from the conduction band to the valence band, leading to electron-hole recombination. In many crystals, this transition occurs via intermediate luminescent centers, whose energy levels lie in the forbidden band. These centers are created by defects or impurity atoms in the crystal. During the two-stage transition, photons are emitted with energy lower than the forbidden band width. Since these photons have a low probability of absorption within the crystal, the light output is significantly higher than in pure, impurity-free crystals.

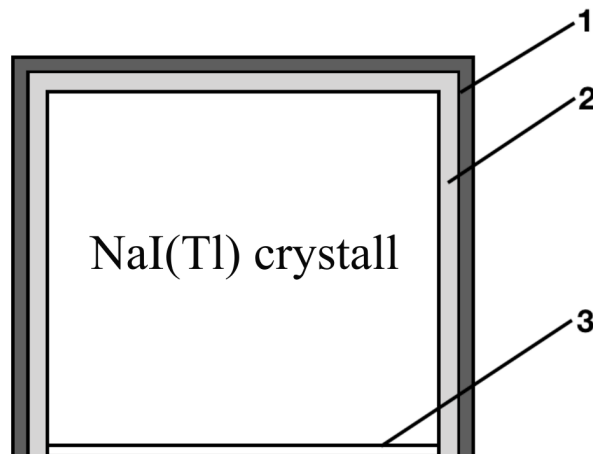


Figure 3.7: Crystal packaging;1 – duralumin housing;2 – magnesium oxide reflector;3 – glass.

**Organic Crystalline Scintillators.** The molecular bonding forces in organic crystals are relatively weak compared to those in inorganic crystals. As a result, interacting molecules hardly disturb each other's electronic energy levels, and the luminescence process of an organic crystal is a process characteristic of individual molecules. In its ground electronic state, a molecule has several vibrational levels. Upon interaction with the detected radiation, the molecule transitions to an excited electronic state, which also corresponds to multiple vibrational levels. Ionization and molecular dissociation are also possible. After recombination,

the ionized molecule typically remains in an excited state. Initially, the excited molecule may occupy high-energy levels and, within a short time ( $\sim 10^{-11}$  s), emit a high-energy photon. This photon is absorbed by another molecule, where part of the excitation energy may be dissipated as thermal motion. The subsequently emitted photon will then have less energy than the preceding one. After several cycles of emission and absorption, molecules end up in the first excited level, emitting photons whose energy is insufficient to excite other molecules. As a result, the crystal remains transparent to the emitted radiation.

Since a significant portion of the excitation energy is converted into thermal motion, the light yield (conversion efficiency) of the crystal is relatively low – only a few percent.

Solid organic scintillators often include single crystals of anthracene ( $C_{14}H_{10}$ ), stilbene ( $C_{14}H_{12}$ ), naphthalene ( $C_{10}H_8$ ) with anthracene (5%), tolane (diphenylacetylene), and others. Compared to inorganic scintillators, all organic scintillators exhibit shorter decay times and lower density. Detectors based on organic crystals offer excellent timing resolution, typically in the range of  $10^{-6}$  to  $10^{-8}$  s, but have lower efficiency for  $\gamma$ -radiation detection.

These scintillators are commonly used in various configurations for detecting and spectrometry  $\alpha$ - and  $\beta$ -particles. For instance, single crystals of stilbene and tolane can be grown to large sizes with relatively short decay times. Stilbene, although having a slightly lower light yield than anthracene, features a significantly shorter scintillation duration  $\sim 7 \cdot 10^{-9}$  s. This characteristic makes stilbene particularly suitable for experiments requiring the detection of highly intense radiation.

**Plastic Scintillators.** Plastic scintillators are solid solutions of fluorescent organic compounds (n-Terphenyl, 2,5-Diphenyloxazole, 1-Phenyl-2-[4-biphenyl]-ethylene, etc.) in a suitable transparent substance. For example, solutions of anthracene or stilbene in polystyrene or plexiglass. The concentrations of the dissolved fluorescent substance are usually small and amount to a few tenths of a percent or a few percent. Since the solvent is much more abundant than the dissolved scintillator, it is natural that the detected particle primarily excites the molecules of the solvent. The excitation energy is subsequently transferred to the molecules of the scintillator. It is obvious that the emission spectrum of the solvent should be more energetic than the absorption spectrum of the dissolved substance, or at least coincide with it. Experimental facts show that the excitation energy of the solvent is transferred to the molecules of the scintillator through a photon

mechanism, i.e., the solvent molecules emit photons, which are then absorbed by the molecules of the dissolved substance. Another energy transfer mechanism is also possible. Since the concentration of the scintillator is low, the solution remains practically transparent to the emitted radiation of the scintillator.

Plastic scintillators are characterized by: a short decay time on the order of  $10^{-8} - 10^{-9}$  sec, satisfactory resistance to radiation exposure, and a proportional dependence of the scintillation pulse heights on the energy of the radiation. The scintillation efficiency of the best plastic scintillators reaches 70% of the efficiency of stilbene monocrystals. A valuable property of plastic scintillators is their transparency to their own radiation.

Scintillating plastics are easily manufactured, mechanically processed, and produce intense luminescence. As an example, solid solutions of terphenyl or anthracene in polystyrene can be mentioned. Phosphor plastics can be produced in large volumes and any shape (block detectors, films, capillaries, etc.). Plastic scintillating detectors have lower efficiencies than the introduced scintillator substance due to its lower concentration per unit volume of the detector. However, such detectors are not afraid of mechanical impacts, moisture, and can operate in a temperature range of  $(-190^{\circ}\text{C} - +70^{\circ}\text{C})$ . They are used for detecting charged particles. They are also sensitive to  $\gamma$ -radiation.

Organic scintillators in crystalline and polymerized forms are used for detecting fast neutrons due to the effect of their elastic scattering in the detector material and the resulting recoil nuclei. However, in each case, the degree of influence of the accompanying  $\gamma$ -radiation on the neutron flux should be assessed.

**Liquid Organic Scintillators** are solutions of fluorescent substances in transparent solvents that weakly absorb radiation energy in the violet and ultraviolet parts of the spectrum. The solvents include purified m-xylene, toluene, phenylcyclohexane, with scintillating additives such as n-Terphenyl, 2,5-Diphenyloxazole (PPO), 1,4-Di-[2-(5-phenyloxazolyl)]-benzene (POPOP), 2,5-Di-(1-naphthyl)-1,3,4-oxadiazole, 1-Phenyl-2-(4-biphenyl)-ethylene, Quaterphenyl, and others. The scintillator with the highest light output is made by dissolving p-terphenyl in xylene at a concentration of 5 g/L.

A valuable property of liquid scintillators is their short decay time ( $10^{-8} - 10^{-9}$  sec), good transparency to their own radiation, and the ability to produce them in any volume and container.

The fluorescence mechanism in liquid scintillators is similar to that in solid scintillators.

The use of liquids allows for unlimited volumes of phosphors. A liquid detector typically consists of a glass vessel, matching the diameter of the photomultiplier tube (PMT) cathode, filled with a scintillating solution and placed directly on the photocathode of the PMT. The radioactive sample to be measured is placed inside the liquid volume or mixed with the liquid scintillator. To increase the efficiency of such a liquid counter, the emission spectrum maximum of paraterphenyl is shifted toward the sensitivity maximum of the PMT photocathode by adding so-called "shifting additives" to the scintillator solution in recommended proportions. Standard preparations such as POPOP, PPO, etc., are often used as such additives. Liquid scintillation detectors are widely used in radiometry of samples containing low-energy  $\beta$ -particles. They are also used for detecting  $\gamma$ -radiation and neutrons. In the latter case, a substance is dissolved in organic liquids in which neutrons induce a nuclear reaction producing a charged particle.

However, in high neutron fluxes (more than  $10^{12}$  neutrons/cm<sup>2</sup>/sec), detectors based on traditional organic solvents practically fail. For operation in high neutron fluxes, a flow-type neutron scintillation detector is used, which employs the well-known nuclear reaction  ${}^6\text{Li} + n \rightarrow \alpha + \text{T}$ . The detector consists of a  ${}^6\text{Li}$  ( $3 \times 3$  mm) with a thickness of  $10 \mu\text{m}$ , enclosed in a Mylar shell  $1 \mu\text{m}$  thick, which serves to isolate the lithium from the environment and create a structure (placed in an aluminum frame) that is washed on both sides by a flow of a fluorine-containing liquid scintillator. The scintillation light from each side is directed through its light guide to the photocathode of its PMT. The directions of the scintillator flow, neutron flow, and the light flow to the PMT are mutually perpendicular, which, in principle, allows shielding the PMT from neutron irradiation. As a result of the nuclear reaction on  ${}^6\text{Li}$   $\alpha$ -particle and tritium are detected on opposite sides of the  ${}^6\text{Li}$  film (in different volumes of the scintillator) by their respective PMTs, which are connected in coincidence, significantly reducing the background.

The concentration of the fluorescent substance is usually low, and the detected particle primarily excites the molecules of the solvent. Subsequently, the excitation energy is transferred to the molecules of the fluorescent substance. Liquid scintillation measurement techniques are widely developed, where radioactive substances are introduced (dissolved, emulsified, etc.) directly into the liquid scintillation mixture. This ensures simplicity in sample preparation, favorable geometric measurement conditions, and eliminates losses associated with radiation attenuation.

Since molecular levels are excited in organic scintillators, which emit in the

Table 3.1: Characteristics of Some Solid and Liquid Scintillators Used in Scintillation Counters

Substance	Density, g/cm <sup>3</sup>	Decay Time, t, 10 <sup>-9</sup> sec	Wavelength at Spectrum Maximum, nm	Conversion Efficiency h,% (for electrons)
<b>Crystals</b>				
Anthracene C <sub>14</sub> H <sub>10</sub>	1.25	30	445	4
Stilbene C <sub>14</sub> H <sub>12</sub>	1.16	6	410	3
NaI(Tl)	3.67	250	410	6
ZnS(Ag)	4.09	11	450	10
CsI(Tl)	4.5	700	560	2
<b>Liquids</b>				
Solution of p-terphenyl in xylene (5 g/L) with POPOP (0.1 g/L)	0.86	2	350	2
Solution of p-terphenyl in toluene (4 g/L) with POPOP (0.1 g/L)	0.86	2.7	430	2.5
<b>Plastics</b>				
Polystyrene with p-terphenyl (0.9%) and a-NPO (0.05 wt%)	1.06	2.2	400	1.6
Polyvinyltoluene with 3.4% p-terphenyl and 0.1 wt% POPOP	1.1	3	430	2

ultraviolet region, wavelength shifters are used to match the spectral sensitivity of light detectors (PMTs and photodiodes). These shifters absorb ultraviolet radiation and re-emit visible light in the region of 400 nm.

**Gas Scintillators.** When charged particles pass through various gases, scintillations are observed. The highest light yield is exhibited by heavy noble gases (xenon and krypton). A mixture of xenon and helium also has a high light yield. The presence of 10% xenon in helium provides a light yield even greater than that of pure xenon. Trace impurities of other gases sharply reduce the intensity of scintillations in noble gases.

Table 3.2: Characteristics of some gases used as scintillators in scintillation counters (at a pressure of 740 mmHg, for  $\alpha$ -particles with an energy of 4.7 MeV)

Gas	Decay time, t, sec	Wavelength at the spectrum maxi- mum, nm	Conversion effi- ciency n,%
Xenon	10 <sup>-8</sup>	325	14
Krypton	10 <sup>-8</sup>	318	8.7
Argon	10 <sup>-8</sup>	250	3
Nitrogen	3·10 <sup>-9</sup>	390	2

For the study of low-energy charged particles ( $> 0.1$  MeV) and nuclear fission fragments, gases (Table 3.2) are used as scintillators, primarily noble gases (Xe, Kr, Ar, He), with xenon being the main one. In this case, the photocathode of the photomultiplier is placed in a corresponding light-isolated gas-filled volume. The radioactive object being measured is also placed in this gas-filled volume. The emission spectra of these noble gases lie in the violet region of the spectrum.

Experimentally, it has been shown that the duration of flashes in noble gases is short ( $10^{-9}$ – $10^{-8}$  sec), and the intensity of flashes is proportional to the energy loss of the detected particles over a wide range and does not depend on their mass or charge. Gas scintillators have low sensitivity to  $\gamma$ -radiation.

Gases exhibit a linear dependence of the signal magnitude on the particle energy over a wide energy range, fast response, and the ability to change the stopping power by adjusting the pressure. Additionally, the source can be introduced into the volume of the gas scintillator. However, gas scintillators require high gas purity and a special photomultiplier tube (PMT) with quartz windows (a significant portion of the emitted light lies in the ultraviolet region).

The main characteristics of scintillators are: the emission spectrum, determined by the probability of emitting photons of a given wavelength; light yield – the ratio of the average number of photons per scintillation to the energy lost by the particle during deceleration; energy yield – the ratio of the total energy of photons per scintillation to the energy lost by the particle during deceleration; decay time – the time during which the intensity of an individual scintillation decreases by a factor of  $e$ . All characteristics of scintillators depend on their chemical composition, size, and degree of purity.

Light yield – the fraction of the energy of the detected particle converted into the energy of a light flash. The light yield of anthracene is  $\sim 0.05$  or 1 photon per 50 eV for high-energy particles. For NaI, the light yield is  $\sim 0.1$  or 1 photon per 25 eV. It is common to compare the light yield of a given scintillator with that of anthracene, which is used as a standard. Typical light yields of plastic scintillators are 50-60%.

### 3.3 Photomultiplier Tube

The light pulse generated in the scintillator upon the passage of an ionizing particle through it is detected using a photomultiplier tube (PMT). When photons pass through the transparent window and hit the photocathode of the PMT, they eject

a certain number of electrons from the photosensitive layer. These photoelectrons are accelerated and focused by an electric field in a vacuum so that they hit a special electrode called a dynode. The dynode is made of a material with a low work function, capable of emitting secondary electrons in quantities several times greater than the number of primary electrons. The electrons emitted from the dynode are again accelerated by the electric field and directed to the next dynode, which also acts as an emitter of secondary electrons. The number of dynodes or emitters in a photomultiplier tube can be quite large ( $\sim 10$ ). As the electrons move from one dynode to the next, the number of electrons in each subsequent generation increases and, depending on the properties and number of dynodes, can exceed the initial number of electrons generated by the photoelectric effect at the cathode by several orders of magnitude. When the electron beam passes between the last dynode and the collecting electrode, called the collector or anode, an electric current pulse is generated in the external circuit of the PMT, which is detected by the corresponding electronic device [14].

### 3.3.1 Photocathode

Photomultipliers use photocathodes of complex composition, which exhibit high sensitivity in the visible light region, as well as in the adjacent ultraviolet and infrared regions. Photocathodes are typically made semi-transparent and are either directly applied to the photomultiplier tube (PMT) bulb or onto a transparent metallic substrate pre-deposited on the glass. The efficiency of photocathodes is characterized either by quantum efficiency (conversion efficiency)  $q$ , integral sensitivity  $\gamma_0$ , or spectral sensitivity  $\gamma(\lambda)$ .

The most comprehensive characteristic of a photocathode is its spectral sensitivity, defined as the ratio of the photocathode current to the photon energy flux at a given wavelength. The value  $\gamma(\lambda)$  is expressed in amperes per watt, or electrons per photon, or amperes per lumen. The relationship between these units is as follows:  $1 \text{ A/W} = 1.24 \cdot 10^{-4}/\lambda \text{ electrons/photon} = 683 \cdot k(\lambda) \text{ A/lm}$ , where  $k(\lambda)$  is the relative luminous efficiency, which ranges from 0 (insensitivity) to 1 (maximum sensitivity).

The integral sensitivity of a photocathode  $\gamma_0$  is the average value of the spectral sensitivity, averaged over the emission spectrum of a standard light source (a 100-watt gas-filled tungsten filament lamp at  $T = 2856 \text{ K}$ ). Naturally, the integral sensitivity of a photocathode varies for light sources with different spectral compositions. The integral sensitivity of photocathodes typically ranges from 10

to  $200 \mu\text{A}/\text{lm}$ .

The quantum efficiency of a photocathode, which represents the probability that a photon will eject an electron from the photocathode, can be defined as  $q = \mu/m$ , where  $\mu$  is the average number of photoelectrons generated by the photoelectric effect and leaving the photocathode, and  $m$  is the average number of incident photons on the photocathode.

The conversion efficiency can be represented as the product of two probabilities: the probability of photon absorption in the photocathode and the probability of electron emission from the photocathode. The former increases with the thickness of the photocathode layer. The mean free path of photons with  $\lambda \sim 300 \text{ nm}$  in an antimony-cesium photocathode is about  $10^{-5} \text{ cm}$ . The probability of electron emission from the photocathode decreases the deeper the electron is generated within the photocathode due to the photoelectric effect. Since the mean free paths of photoelectrons in the photocathode are shorter than those of photons, at small photocathode thicknesses, all photoelectrons can escape the photocathode, but only a small fraction of light is absorbed, and vice versa. Thus, the dependence of the quantum efficiency of a photocathode on its thickness has a maximum.

The most common photocathodes are antimony-cesium (Sb–Cs) and bismuth-silver-cesium (Bi–Ag–Cs) photocathodes, which exhibit the best overlap of spectral sensitivity with the emission spectra of many scintillators.

Complex photocathodes consist of a thin film of several hundred or thousand atomic layers deposited on a metallic or insulating substrate. An antimony-cesium photocathode consists of a layer of  $\text{SbCs}_3$ , within which and on the surface are adsorbed cesium atoms.

There are several properties of photocathodes that must be considered when working with PMTs. Even if the photocathode is completely darkened, electrons still escape from its surface due to thermionic emission. This is inevitable because, to achieve high quantum efficiency, the photocathode must have a low work function, and thermionic emission increases as the work function decreases. The thermionic current of complex photocathodes at room temperature is on the order of  $10^{-14} - 10^{-15} \text{ A}/\text{cm}^2$  or  $10^4 - 10^5$  electrons per  $\text{cm}^2/\text{s}$ . Thermionic emission increases sharply with temperature:  $i \sim T^2 \exp(-\varphi_0/kT)$ , where  $\varphi_0$  is the work function;  $T$  is the temperature.

The integral sensitivity of complex photocathodes decreases noticeably with increasing temperature. For example, for antimony-cesium photocathodes, the photocurrent decreases by a factor of 1.2 to 1.5 when the temperature changes

from 0 to 100 °C. The change in photocurrent with decreasing temperature depends on the photocathode design. Photocathodes deposited on a metallic film are insensitive to temperature changes from 0 to -200 °C. However, the photocurrent drops sharply with decreasing temperature (by a factor of 10 when changing from 0 to -200 °C) for photocathodes deposited on glass.

The integral sensitivity (along with spectral sensitivity and quantum efficiency) of photocathodes generally decreases during operation, and the greater the light flux and the longer the photocathode is illuminated, the more its sensitivity decreases. This phenomenon is called photocathode fatigue and is associated with processes occurring in its surface layer. When the photocathode is irradiated, some of the alkali metal ions formed on the surface due to photoionization of atoms diffuse into the cathode under the influence of the electric field. This process is possible because instantaneous recombination is hindered by the poor conductivity of the inner layers of the photocathode. As a result, when the photocathode is illuminated, the surface becomes depleted of cesium atoms, leading to an increase in the work function and, consequently, a decrease in photocurrent. The movement of cesium ions into the photocathode is more intense the more light falls on the photocathode and the greater the potential difference across the photocathode. With this fatigue mechanism, the sensitivity of photocathodes recovers after a long "rest," during which cesium atoms diffuse from the inner layers to the cathode surface.

The qualitative picture of photocathode fatigue is confirmed experimentally. Moreover, the recovery of photocathode sensitivity occurs faster at higher temperatures.

Electrons leave the photocathode with different velocities and at different angles to the cathode surface. The design of the PMT input chamber should be such that the collection of electrons on the first dynode is as large and uniform as possible from different areas of the photocathode. The fewer electrons that reach the first dynode, the greater the relative fluctuation in their number and the greater the spread in pulse amplitudes at the PMT output. Non-uniform electron collection from different areas of the photocathode also increases the fluctuations in pulse amplitudes. In PMTs with large photocathodes, the input chamber has larger dimensions, complicating the focusing of photoelectrons on the first dynode. In such cases, focusing is achieved using an electric field created by two or three ring electrodes in the input chamber.

### 3.3.2 Dynode System of PMT

The dynode system in a PMT is designed to amplify electron flows. Electron multiplication at each dynode occurs due to secondary emission. The electron multiplication process is effective if, firstly, the secondary emission coefficient is greater than one, and secondly, if the collection of secondary emission electrons from the previous dynode to the subsequent one is as complete as possible.

Secondary electron emission is characterized by the secondary emission coefficient: the ratio of the secondary electron current to the primary electron current. The secondary emission coefficient  $\beta$  depends on the material and its surface condition, the energy of the primary electrons, and the angle of incidence of the electrons. The secondary emission coefficient initially increases with the energy of the electrons and then decreases. This is because electrons, upon entering the material, transfer their energy to many electrons through elastic and inelastic collisions. The higher the energy of the primary electron, the more electrons it transfers energy to. However, on the other hand, the higher the energy of the primary electron, the deeper it penetrates, and thus the secondary electrons acquire energy at a greater depth within the material, reducing their probability of escaping the material. Therefore, the dependence of the secondary emission coefficient on the energy of the incident electrons has a maximum.

If the process of energy transfer to secondary electrons is mainly determined by the energy of the primary electron, the movement of secondary electrons to the surface of the dynode and their escape from the material is primarily determined by the material itself (metal, dielectric, semiconductor). The intense interaction of secondary electrons with conduction electrons is the main reason for the low secondary emission coefficient in metals. In semiconductors and dielectrics, secondary electrons have a higher probability of escaping. However, the secondary emission coefficient is not higher for all semiconductors and dielectrics compared to metals. The work function of these materials, which hinders the removal of secondary electrons from the material, also plays a role.

The secondary emission coefficient  $\beta$  significantly depends on the angle of incidence of the primary electrons. The greater the angle at which electrons strike the material surface, the higher  $\beta$ . This dependence of  $\beta$  on the angle of incidence is due to the fact that at larger angles of incidence, secondary electrons are generated closer to the material surface. The energy distribution of secondary electrons weakly depends on the energy of the primary electrons.

The maximum values  $\beta_{max}$  for metals range from 0.5 to 1.8 and are achieved at

electron energies of 100–800 eV (depending on the material). Significantly higher  $\beta_{max}$  values are obtained for complex compounds such as Sb – Cs, Cu – S – Cs, Ag – Mg. These are achieved at electron energies near 1 keV and are equal to  $7\div 10$ .

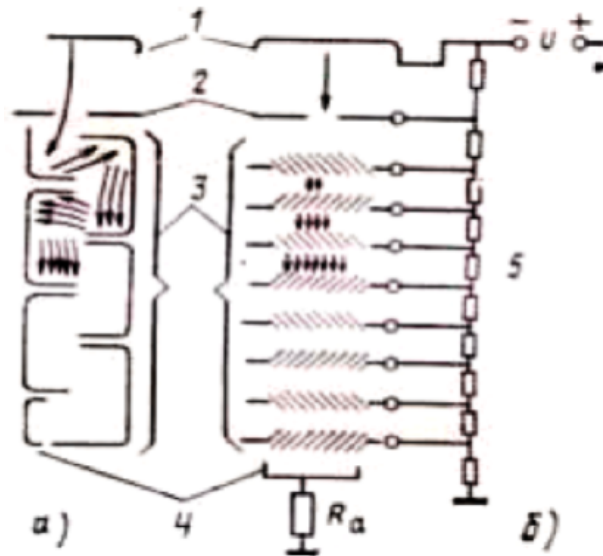


Figure 3.8: Schemes of dynode system arrangements: a) box-type and b) venetian-blind type. 1 - photocathodes, 2 - diaphragms, 3 - dynodes, 4 - anodes, 5 - voltage dividers,  $R_a$  - anode load [12]

In modern PMTs, dynodes are coated with a layer of Sb - Cs or use alloys such as Al - Mg - Si, Mg - O - Cs, whose surfaces are specially treated to increase  $\beta$  [2].

PMT dynodes come in various shapes and can be divided into two groups: focusing dynodes and venetian-blind type dynodes. Focusing dynodes come in different configurations: box-type, box-and-grid type, etc. Figure ?? shows the arrangement of box-type (a) and venetian-blind type (b) PMTs. As an example, box-type dynodes are used in PMTs such as: domestic – FEU-29, FEU-24, foreign – Hamamatsu R375, R562, R1017, while venetian-blind type dynodes are used in: domestic – FEU-11 and FEU-43, foreign – Hamamatsu R2218, R1408, R1449 [11].

There are also more advanced dynode systems – with linear focusing, used, for example, in Hamamatsu R943-02, R2497, R2080, R5600, and circular types such as Hamamatsu R106UH, R2693 [11].

The number of dynodes in a PMT is usually  $10\div 14$ . A potential difference is created between the dynodes using an external power supply and a voltage divider (Fig. 3.8).

### 3.3.3 Gain Coefficient

If a PMT has  $N$  dynodes, and the secondary emission coefficient for each of them is  $\beta_i$ , and the collection efficiency is  $n_i$ , then the gain coefficient of the PMT is:

$$M = \prod_{i=1}^N n_i \cdot \beta_i \quad (3.12)$$

The gain coefficient of each dynode fluctuates around the statistical mean. The same applies to the total gain coefficient  $M$  of the PMT, which is determined by a probability distribution with a mean  $\overline{M}$  [13].

The response of the multiplier dynode system (output charge) to a single photoelectron, with a high secondary electron emission coefficient from the first dynode ( $\beta_1 \gg 1$ ) and a collection efficiency close to unity on the first dynodes, can be described by a Gaussian distribution:

$$M(x) = \frac{1}{\sigma_1 \sqrt{2\pi}} \exp\left(-\frac{(x - Q_1)^2}{2\sigma_1^2}\right) \quad (3.13)$$

where  $x$  is the variable (charge),  $Q_1 = \overline{M}e$  ( $e = 1,6 \cdot 10^{-19}$  C) is the average charge at the output of the PMT when one electron is collected on the first dynode, and  $\sigma_1$  is the standard deviation of the charge distribution [5].

Gain fluctuations can be reduced by:

- increasing the secondary emission coefficient,
- improving the uniformity of the secondary emission coefficient,
- stabilizing the collection efficiency on the dynodes [13].

The gain coefficient also depends on many external factors: voltage, temperature, and magnetic field strength. Since  $M$  is highly dependent on the supply voltage, the voltage sources must have high stability [2]. The gain coefficient of the PMT can change by  $\pm 0.5\%$  with a temperature change of  $1^\circ\text{C}$ . The magnetic field affects PMTs that have focusing electrodes and where electron focusing from dynode to dynode is performed. The magnetic field can also affect PMTs if they are not shielded. Venetian-blind PMTs are practically insensitive to magnetic fields up to a strength of several tens of amperes per meter.

### 3.3.4 PMT Noise

At the output of a completely darkened PMT under voltage, there are always noise pulses. Their occurrence is due to: 1) thermionic emission from the photocathode

and dynodes; 2) leakage current fluctuations; 3) auto-electronic (cold) emission; 4) ion and optical feedback; and 5) radioactivity.

Let us consider the main sources of noise.

At normal temperature, approximately  $10^5$  electrons are emitted per second from  $1 \text{ cm}^2$  of an antimony-cesium photocathode due to thermionic emission. Consequently, at the output of the PMT, there will be approximately  $10^6$  pulses per second (if the cathode area is about  $10 \text{ cm}^2$ ) with an amplitude of approximately  $Me/C$  (where  $C$  is the capacitance of the PMT anode circuit). The contribution of thermionic emission from the dynodes to the noise is smaller. This is because the amplitude of the pulse at the PMT anode, created by a thermoelectron from each subsequent dynode, decreases by a factor of  $\beta$ .

Noise pulses also arise due to leakage current. The insulation resistance between the anode and other electrodes in the PMT at normal temperature is  $10^8 - 10^9$  Ohms. At voltages of about (1-2) kV, the leakage current is 1-20  $\mu\text{A}$ . This corresponds to fluctuations in the number of charges of  $10^3 - 10^4$  in a time interval of about  $\tau = 10^{-6}$  s. Such amplitudes are significant when the PMT gain is less than or on the order of  $10^4$  [2].

## Chapter 4

# Experimental Setup

The study of various radiation sources is conducted using a setup, the schematic of which is shown in Fig. 4.1.

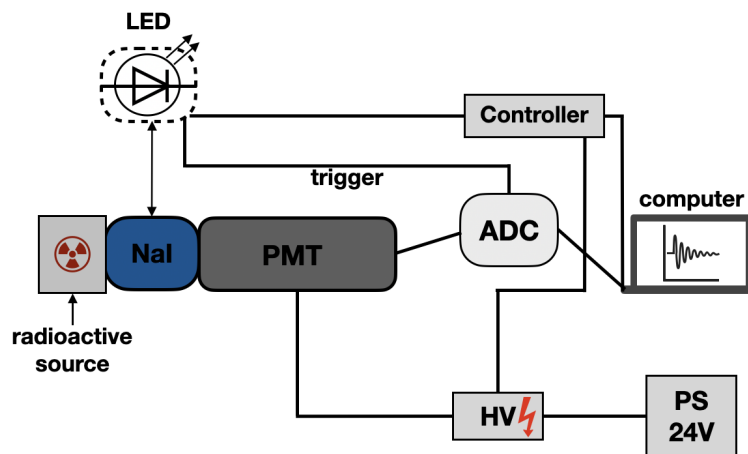


Figure 4.1: Schematic of the experimental setup

A NaI scintillator is used as the gamma-ray detector, mounted in a special housing that connects to the photodetector – a photomultiplier tube (PMT) EMI 9839A. A gamma-ray passing through the scintillator loses all or part of its energy in it. During this process, a light flash occurs in the scintillator, the intensity of which depends on the amount of energy deposited. The light is detected by the PMT, and the signal from it is sent to an analog-to-digital converter (ADC). The ADC used is the DRS4 board, developed at PSI (Switzerland). To record the signal from the ADC to a personal computer, specialized software is used (see Fig. 4.3), which allows changing various ADC parameters and recording settings, as well as providing online signal visualization – an oscilloscope analog with the ability to process and analyze the signal, including histogram construction. The PMT is powered by a high-voltage module developed by HVSys [7], which also requires a 24 V power supply, provided by a specialized power supply.

Before proceeding with data collection from a radioactive source, it is necessary to calibrate the PMT to determine its response to the detection of a single photon. For this purpose, the method of low-intensity light flashes is used [3]. A special pulsed self-stabilized light source based on an LED ( $\lambda = 425 \text{ nm}$ ) from HVSys [6] (developed by JINR) is used as the light source, controlled by specialized software (see Fig. 4.2b). By replacing the scintillator with this light source, the PMT calibration is performed.

## 4.1 Software

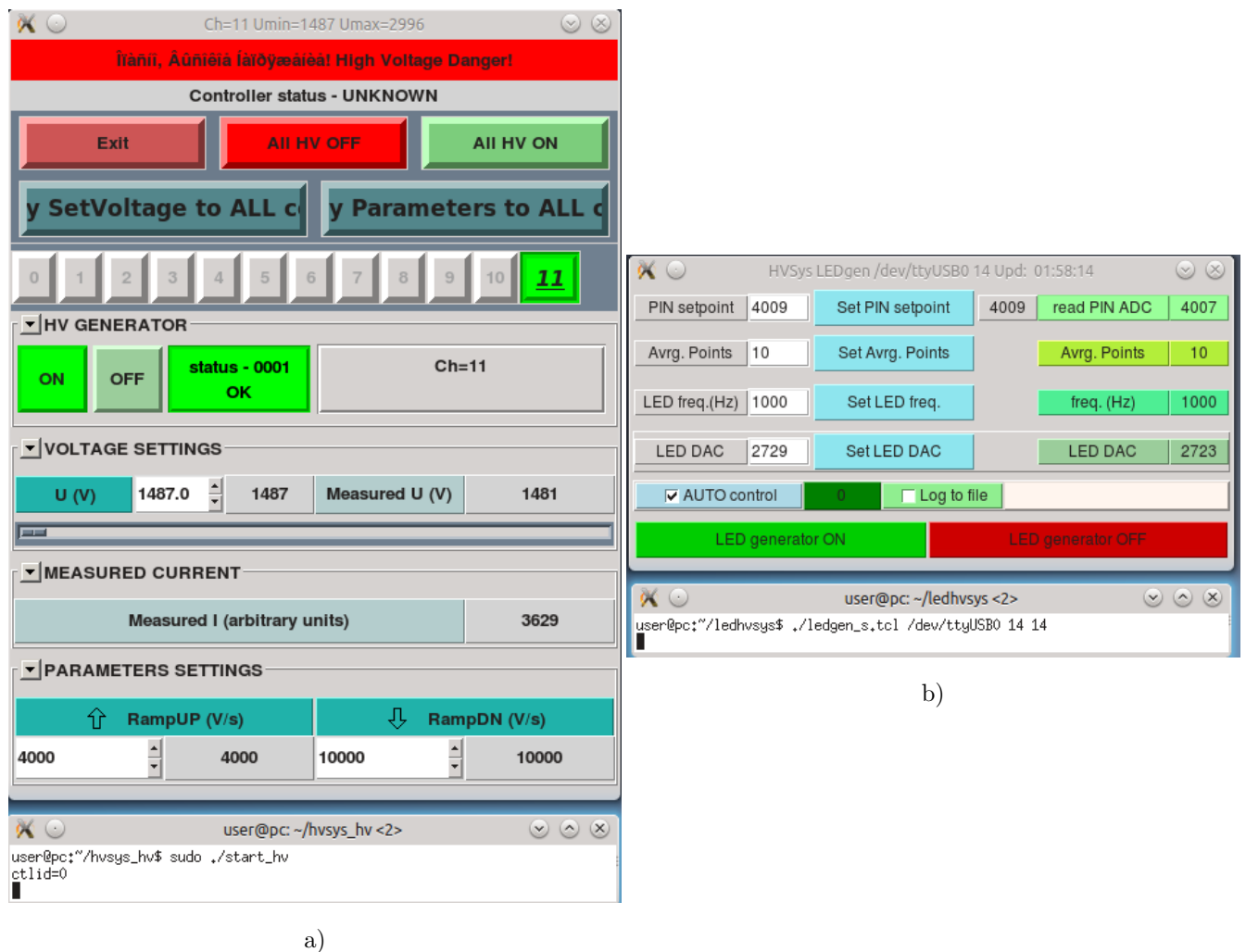


Figure 4.2: Control windows for high-voltage power supply (a) and LED (b)

The high-voltage module from HVSys can provide power ranging from hundreds of volts to 5 kV with a current limit of up to 1 mA. The software for controlling this module is launched from the Linux OS terminal using the command [`sudo ./start_hv`], after which the control window will open (see Fig. 4.2a). In the **Voltage Setting** tab of the control window, the desired voltage value is set (1487 V in Fig. 4.2a), which is applied by pressing **Enter** on the computer keyboard.

Then, in the **HV Generator**, the high voltage is turned on by pressing the **ON** button, supplying high voltage to the output cable of the high-voltage module. To turn off the high voltage, press the **OFF** or **ALL HV OFF** button (red button in Fig. 4.2a). When working with such a power supply, safety precautions must be followed, and instructions from supervisors must be adhered to.

Similarly, to launch the LED control window (see Fig. 4.2b), the command `./ledgen_s.tcl /det/ttyUSB $N$   $X$   $Y$`  must be executed in the Linux OS terminal, where  $N$  is the number of the USB port to which the LED controller is connected, and  $X$  and  $Y$  are the initial and final numbers of the LEDs, respectively, among which the connected devices are searched and initialized. The control window has several settings that need to be configured during the first launch of the LED, as well as control buttons:

- **PIN setpoint** - the light level on the PIN diode in arbitrary units from  $\text{min} = 10$  to  $\text{max} = 4096$ . Since the PIN diode operates in feedback with the LED, this setting also regulates the light output of the LED.
- **Avrg. Points** - The number of averaging points for the signal from the PIN diode in the feedback circuit (usually from 10–100).
- **LED freq.(Hz)** - The frequency of light pulses from the LED in Hz.
- **LED DAC** - The pulse magnitude on the LED in arbitrary units from  $\text{min} = 10$  to  $\text{max} = 4096$ .
- **AUTO control** - Controls the feedback mode – self-regulation of the LED light output. If enabled, the LED light is set according to the PIN setpoint; otherwise, it is set according to the LED DAC.
- **LED generator ON** and **LED generator OFF** - Buttons to turn the LED on and off.

To work with the DRS4 ADC, software is installed from the manufacturer's website [8] (Fig. 4.3). The software is launched in the Linux OS terminal using the command `[drsosc]`. The DRS4 has 4 channels for signal recording and additional trigger logic channels. The control window (see Fig. 4.3) has the following main buttons and options:

- **Stop/Start** - Stop/start signal acquisition.
- **1, 2, 3, or 4** - Buttons to turn channels 1, 2, 3, and 4 on or off.
- **Normal and Auto** - Selection of the trigger mode.

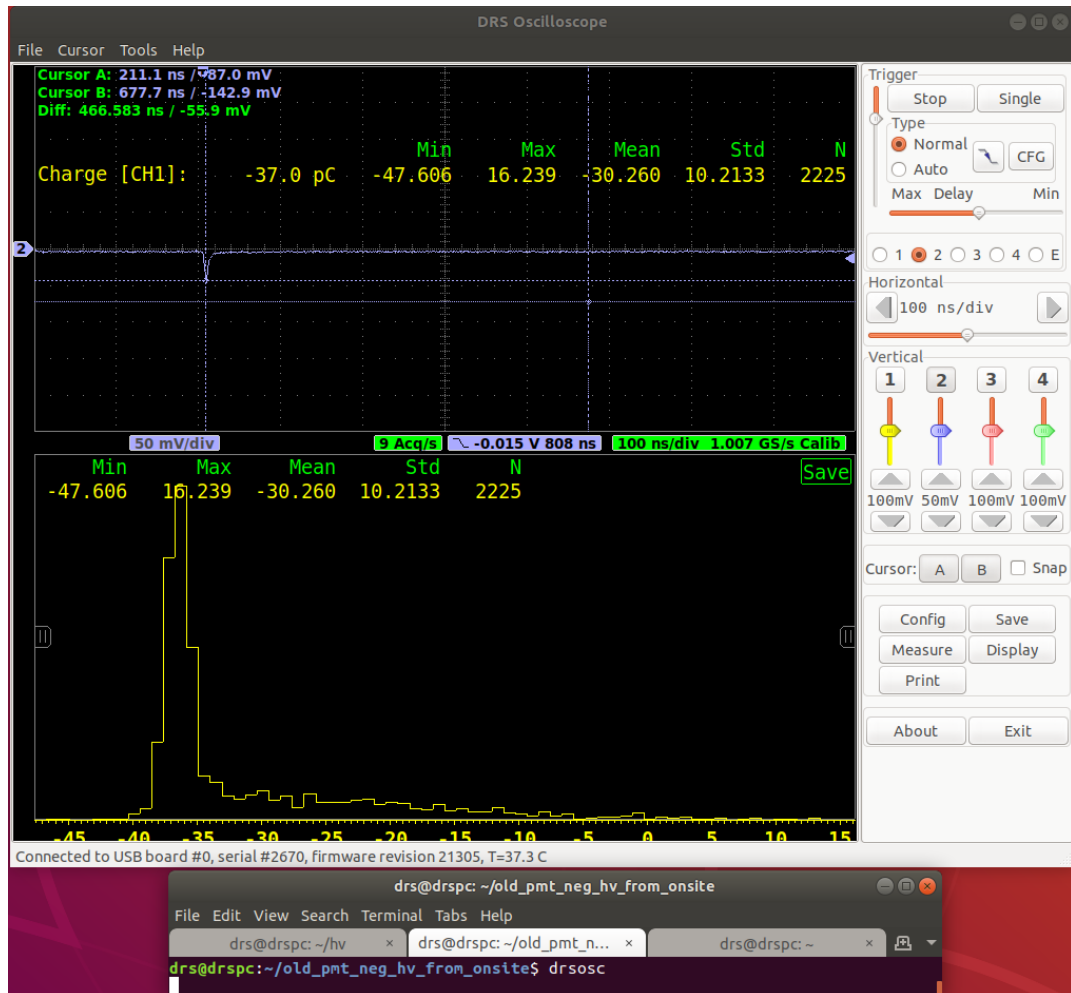


Figure 4.3: ADC control window

- **Trigger (slider) or CFG** - Setting the trigger threshold.
- **Delay (slider)** - Setting the delay between the trigger and the signal.
- **Horizontal (arrows)** - Selection of the sampling rate and, accordingly, the time window width for visualization.
- **Config** - Calibration of the ADC before the first launch.
- **Measure** - Selection of the signal analysis mode (amplitude or charge), as well as the display of statistics and histograms.
- **Cursor: A or B** - Selection of the cursor for setting the analysis range.
- **Save** - Saving data to the computer.

For processing data acquired with the DRS4, specialized software DRSViewer (developed by JINR) is used, which allows for advanced data analysis. This software is launched in the Linux OS terminal using the command [**DRSViewer**]. After launching, the control window will appear (Fig. 4.4), where two main tabs are used:

- **Gate Viewer tab** - Plotting single and average signals, and selecting the integration window for charge spectrum construction.
- **Spectra Creator tab** - Constructing the charge spectrum with numerous additional settings.
- **Save button (Spectra Creator tab)** - Opens a dialog box for saving the spectrum file. The file should be saved in \*.root format.

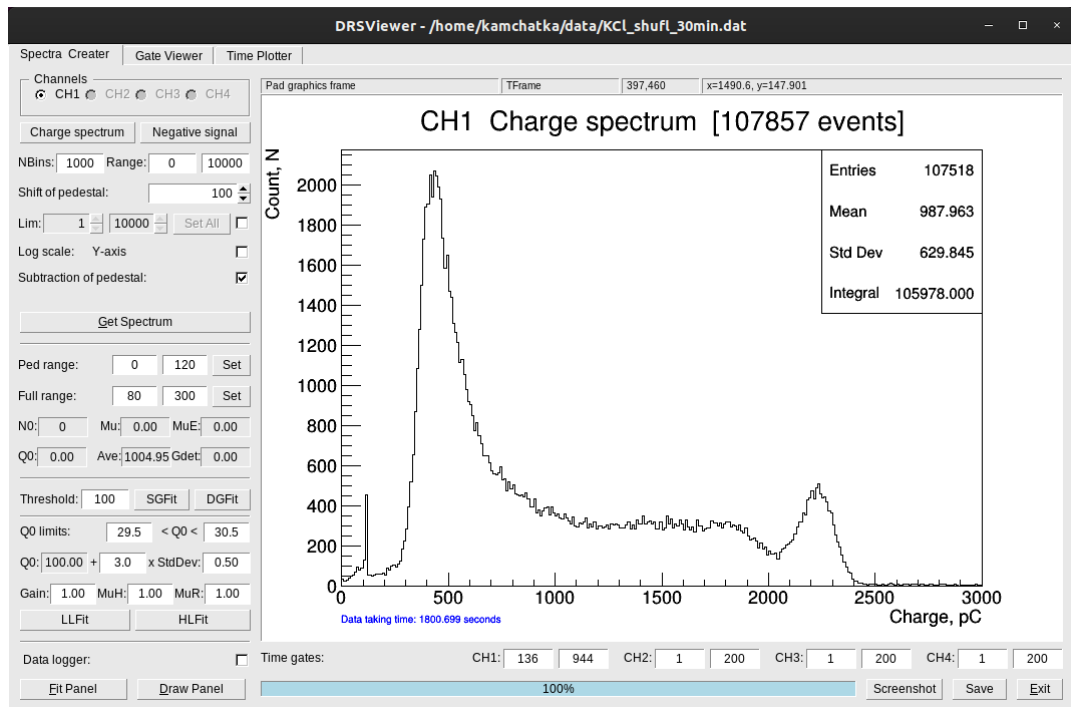


Figure 4.4: Window of the DRSViewer program for data processing

## 4.2 Laboratory Practical. Work Procedure

Using the example of studying the spectrum of potassium chloride-based fertilizer, the sequence of actions for performing the laboratory work is described below.

To begin the laboratory work, it is necessary to assemble the setup (see Fig. 4.1) in the PMT calibration configuration (replace the scintillator and install the light source). Then, connect and configure all elements of the setup: turn on the PMT power supply, set the light intensity on the light source, and configure the ADC for signal recording. After selecting the appropriate light intensity (approximately 1 photoelectron), data acquisition and calibration of the PMT response to a single photoelectron are performed. Here, it is required to calculate the gain of the photodetector in charge units (see Fig. 4.5):

$$G_{pmt} = P_1 - Q_0 = 100.632 - 100.080 = 0.552 \text{ pC}, \quad (4.1)$$

where  $Q_o$  and  $P_1$  are the positions of the pedestal and the single-photoelectron signal of the PMT, and  $G_{pmt}$  is the PMT gain. By determining the PMT gain, we know the value of the spectrometric channel in charge units or photoelectrons when working with radioactive sources.

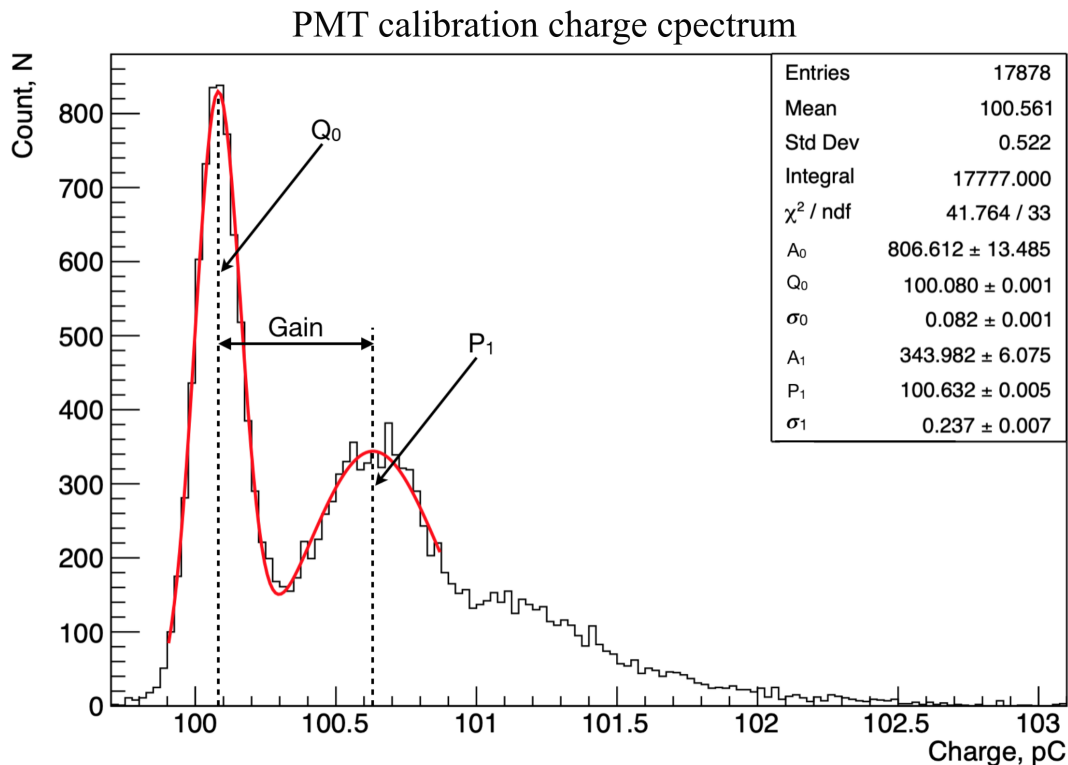


Figure 4.5: Single-photoelectron charge spectrum of the PMT

Before starting data acquisition from the source, it is necessary to set the ADC trigger threshold above the PMT noise level. Place the radioactive source near the scintillator; in the case of potassium chloride, wrap it around the NaI to ensure maximum detection efficiency of  $\gamma$ -quanta from  $^{40}\text{K}$ . Begin data acquisition for a fixed period of time (10 minutes = 600 seconds). Then, repeat the same procedure but without the radioactive source to obtain data on the natural radioactive background. It is important to maintain the same data acquisition time interval.

Figure 4.6(a) shows the spectra from potassium chloride and the natural background acquired over 30 minutes. The full-energy peak (photopeak) of  $\gamma$ -quanta with energy  $E = 1.46 \text{ MeV}$  from  $^{40}\text{K}$  is clearly visible. Figure 4.6(b) demonstrates the spectrum after subtracting the natural background. To perform the subtraction, both spectra must be saved in \*.root format, and the script [root bs.cpp] must be executed. Before running the script, open the file bs.cpp in an editor and enter the names of both spectrum files.

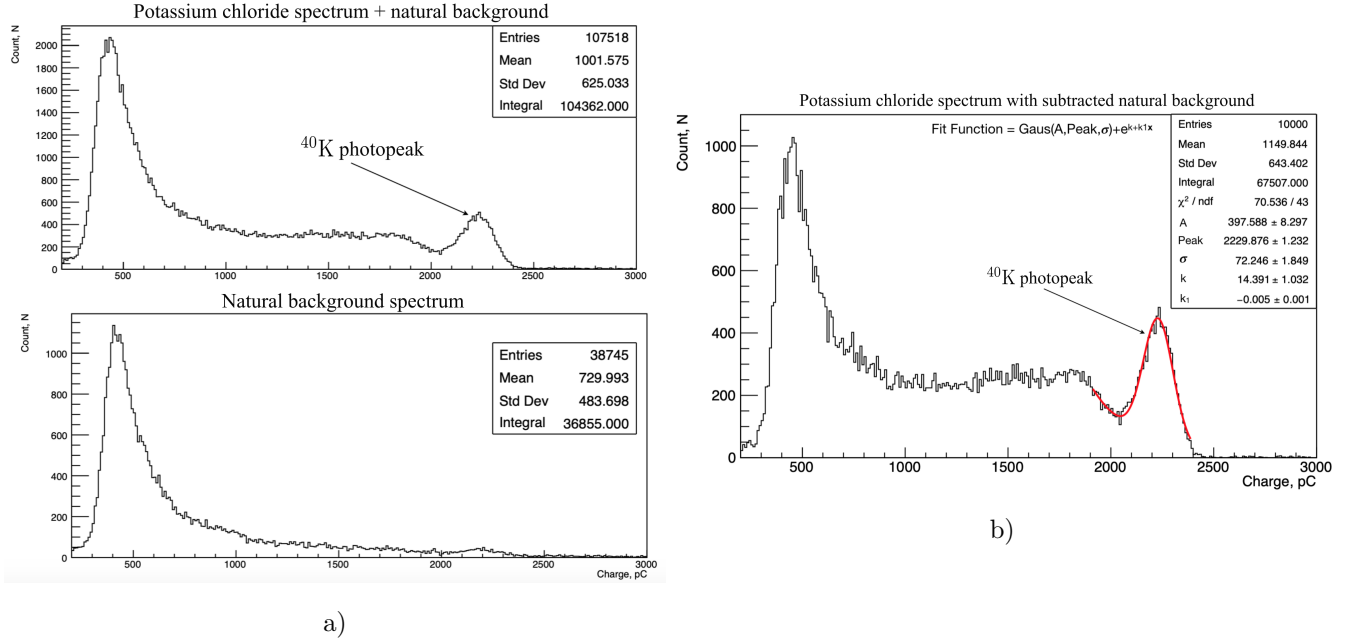


Figure 4.6: Background spectrum, spectrum from potassium chloride, and spectrum after subtracting the natural background

Based on the indicated spectra 4.6, we provide an example of calculating the equivalent dose of natural radiation background. First, determine the channel value in the energy scale and the resolution of the scintillation detector using the spectrum in Fig. 4.6b.

$$P = \text{Peak} - Q_0 = 2229.9 - 100.0 = 2129.9 \text{ pC} \quad (4.2)$$

or

$$P = \frac{2129.9}{G_{pmt}} = \frac{2129.9}{0.552} = 3859 \text{ photoelectrons} \quad (4.3)$$

$$\text{Res} = \frac{2.35 \cdot \sigma}{P} = \frac{2.35 \cdot 72.2}{2129.9} = 0.08(8\%) \quad (4.4)$$

where P is the position of the photopeak from  $^{40}\text{K}$  in picocoulombs or photoelectrons (considering the PMT gain) minus the pedestal position  $Q_0 = 100$ , which is shifted in the software to the 100th channel. Knowing that  $E_\gamma = 1460$  keV (for  $^{40}\text{K}$ ), we obtain:

$$k = \frac{E_\gamma}{P} = \frac{1460}{2129.9} = 0.69 \text{ keV/pC} \quad (4.5)$$

The average energy in the spectrum:

$$E_{\text{av}} = \text{Mean} - Q_0 = (1149.8 - 100.0) \text{ pC} = 1049.8 \text{ pC} \cdot 0.69 \text{ keV/pC} = 724.4 \text{ keV} \quad (4.6)$$

Thus, such a detector effectively registers on average  $\varepsilon_{\text{reg}}$  percent of the energy

from the primary  $\gamma$ -quantum:

$$\varepsilon_{\text{reg}} = \frac{724.4 \text{ keV}}{1460 \text{ keV}} = 0.496 \text{ or } 49.6\% \quad (4.7)$$

The spectrum from the natural background (Fig. 4.6a) shows that the average energy from the background is:

$$E_{\text{av.bkg}} = (730.0 - 100.0) \text{ pC} = 630 \text{ pC} \cdot 0.69 \text{ keV/pC} = 434.7 \text{ keV} \quad (4.8)$$

Taking into account the coefficient  $\varepsilon_{\text{reg}}$ , we can estimate the average energy of background  $\gamma$ -quanta:

$$\langle E_{\text{av.bkg}} \rangle = \frac{E_{\text{av.bkg}}}{\varepsilon_{\text{reg}}} = \frac{434.7}{0.496} = 876.4 \text{ keV} \quad (4.9)$$

It is known that the detection efficiency of  $\gamma$ -quanta by the scintillator depends on their energy and the geometry of the scintillator. In particular, the geometry of the NaI crystal used in the spectrum acquisition was a cylinder with a diameter of 2 inches and the same height. Figure 4.7 shows the absorption efficiency of  $\gamma$ -quanta by NaI crystals of various geometries as a function of energy. For our case, the efficiency is:

$$\text{Eff} \approx 70\% \quad (4.10)$$

It is also necessary to take into account that in our case, this type of ADC (DRS4) has missed counts when recording data to the computer and saves only a part of the signals. To estimate the real count rate, the ADC has a counter mode. Using this mode, the real count rate  $K_{\text{ADC}} = 34 \text{ s}^{-1}$  was obtained. Let us calculate the number of  $\gamma$ -quanta passing through the volume of the NaI crystal:

$$N_{\gamma} = \frac{K_{\text{ADC}}}{\text{Eff}} = \frac{34}{0.7} = 48.6 \text{ s}^{-1} \quad (4.11)$$

Thus, knowing that the volume of the crystal  $V_{\text{cr}} \approx 10^{-4} \text{ m}^3$ , we can estimate the number of background  $\gamma$ -quanta passing through the volume of an average human body. The volume of a human body:

$$V_{\text{hum}} \approx 75 \text{ liters} = 75 \cdot 10^{-3} \text{ m}^3, \quad (4.12)$$

then the number of  $\gamma$ -quanta passing through the human body:

$$N_{\gamma}^{\text{hum}} = \frac{V_{\text{hum}}}{V_{\text{cr}}} \cdot N_{\gamma} = \frac{75 \cdot 10^{-3}}{10^{-4}} \cdot 48.6 \approx 36450 \text{ s}^{-1} \quad (4.13)$$

The energy transfer from  $\gamma$ -quanta to matter follows the following law [9]:

$$I = I_0 \cdot e^{-\mu_k \cdot x}, \quad (4.14)$$

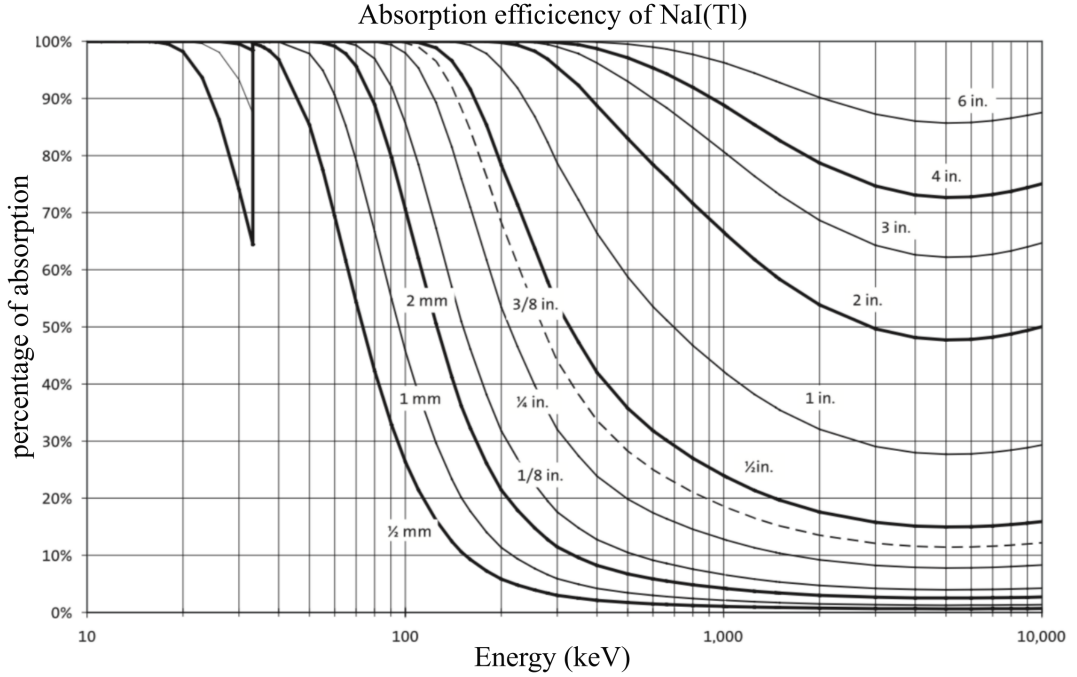


Figure 4.7: Absorption efficiency of  $\gamma$ -quanta for NaI(Tl) [4]

where  $\mu_k$  is the linear energy transfer coefficient of radiation. For a human, primarily composed of water, at  $\gamma$ -quanta energies in the range of 0.1-2 MeV,  $\mu_k \approx 0.030$  (see Table 4.1). Therefore, the fraction of radiation energy deposited in a human  $\varepsilon_{\text{hum}}$  for background  $\gamma$ -quanta, which travel an average of  $\sim 20$  cm in the human body<sup>1</sup>:

$$\varepsilon_{\text{hum}} = 1 - e^{-\mu_k \cdot x} = 1 - e^{-0.030 \cdot 20} = 1 - 0.549 = 0.451 \approx 45\% \quad (4.15)$$

This means that only about 45% of the initial energy of  $\gamma$ -quanta remains in the human body, while the remaining 55% of the energy leaves the body, mainly in the form of secondary (scattered, bremsstrahlung)  $\gamma$ -quanta and partially electrons ejected in the surface layer of the body (skin).<sup>2</sup> We obtain the equivalent dose  $H$  from background  $\gamma$ -quanta passing through a human per unit volume of 1 liter with a mass of 1 kg over a time  $T = 1$  hour = 3600 s:

$$H = w \cdot D, \quad D = E/m, \quad (4.16)$$

$$w = 1 \text{ - for } \gamma\text{-quanta, electrons,} \quad m = 75 \text{ kg,} \quad (4.17)$$

$$E = \varepsilon_{\text{hum}} \cdot \langle E_{\text{av.bkg}} \rangle \cdot T \cdot N_{\text{hum}}, \quad (4.18)$$

<sup>1</sup>This refers to the average across the entire body: torso average diameter is  $\sim 30$  cm, legs  $\sim 15$  cm, arms  $\sim 8$  cm, head  $\sim 20$  cm.

<sup>2</sup>The actual coefficient may be slightly less,  $\sim 40\%$ [10], since the human body is a complex-shaped object, and the photon path slightly reduces the given value.

$$H = 0.451 \cdot 876.4 \cdot 1.6 \cdot 10^{-16} \cdot 3600 \cdot 36450/75 \approx 0.11 \text{ } \mu\text{Sv/h} \quad (4.19)$$

In a similar manner, other types of sources of radiation can be studied, such as volcanic rock, tungsten-thorium welding rods, etc.

Table 4.1: Linear energy transfer coefficients  $\mu_k$  and linear attenuation coefficients  $\mu$  in various media,  $\text{cm}^{-1}$  [9]

Energy of $\gamma$ -quanta, MeV	Water		Aluminum		Lead	
	$\mu_k$	$\mu$	$\mu_k$	$\mu$	$\mu_k$	$\mu$
0.1	0.0253	0.171	0.1002	0.444	24.494	60.0
0.2	0.0299	0.137	0.0742	0.323	6.645	11.8
0.5	0.0330	0.097	0.0775	0.228	1.022	1.72
1.0	0.0310	0.0706	0.0726	0.166	0.435	0.79
2.0	0.0260	0.0493	0.0613	0.117	0.218	0.51
5.0	0.0189	0.0302	0.0486	0.075	0.308	0.49
10.0	0.0154	0.0221	0.0451	0.062	0.372	0.60

# Bibliography

- [1] O.V. Zhurenkov A.A. Chernov. *Geiger-Muller counter*. 2003.
- [2] E.S. Matusevich A.I. Abramov, Yu.A. Kazanski. *Fundamentals of experimental methods of nuclear physics*. Energoatomizdat, Moscow, 1985.
- [3] N. Anfimov, A. Rybnikov, and A. Sotnikov. Optimization of the light intensity for photodetector calibration. *Nuclear Instruments and Methods in Physics Research Section A: Accelerators, Spectrometers, Detectors and Associated Equipment*, 939:61 – 65, 2019.
- [4] Saint-Gobain Crystals. *Efficiency calculations for selected scintillators*, 2019. <https://www.crystals.saint-gobain.com/sites/imdf.crystals.com/files/documents/efficiency-calculations.pdf>.
- [5] E.Bellamy et al. Absolute calibration and monitoring of a spectrometric channel using a photomultiplier. *Nucl. Instr. and Meth. A*, 339:468–476, 1994.
- [6] HVSys. *Calibrated LED sources of light flashes*, 2019. [http://hvsys.ru/images/data/news/5\\_small\\_1368802948.pdf](http://hvsys.ru/images/data/news/5_small_1368802948.pdf).
- [7] HVSys. *igh voltage sources from 0.5 to 15 kV for detectors*, 2019. [http://hvsys.ru/images/data/news/1\\_small\\_1368802771.pdf](http://hvsys.ru/images/data/news/1_small_1368802771.pdf).
- [8] Paul Scherrer Institut. *DRS4 Evaluation Board*, 2019. <https://www.psi.ch/en/drs/evaluation-board>.
- [9] Faculty of General Nuclear Physics of MSU. *Nuclear physics in the Internet*, 2019. [http://nuclphys.sinp.msu.ru/radiation/rad\\_3.htm](http://nuclphys.sinp.msu.ru/radiation/rad_3.htm).
- [10] I.M. Kapitonov Zh.M. Seliverstova A.V. Shumakov O.I Vasilenko, B.S. Ishkhanov. Examples of solving tasks in the textbook «radiation», task no. 3, 2013. <http://nuclphys.sinp.msu.ru/radiation/>.
- [11] Hamamatsu photonics K.K. *Photomultiplier tubes*. Japan, Oct/1990.

- [12] L.S. Stilbans. *Physics of semiconductors*. Soviet radio, Moscow, 1967.
- [13] Photomultiplier tubes principles applications. *Philips Photonick Handbook*. 1994.
- [14] M.S. Kozadaev V.I. Kalashnikova. *Elementary particle detectors*. Nauka, Moscow, 1966.